Journal of Power Sources 195 (2010) 2266–2282

Contents lists available at ScienceDirect

Journal of Power Sources

journal homepage: www.elsevier.com/locate/jpowsour

Elementary reaction kinetic model of an anode-supported solid oxide fuel cell fueled with syngas

Chen Li[a], Yixiang Shi[b], Ningsheng Cai[a,*]

[a] Key laboratory for Thermal Science and Power Engineering of Ministry of Education, Department of Thermal Engineering, Tsinghua University, Beijing 100084, China
[b] Institute of Nuclear and New Energy Technology, Tsinghua University, Beijing 100084, China

ARTICLE INFO

Article history:
Received 15 September 2009
Received in revised form 16 October 2009
Accepted 16 October 2009
Available online 29 October 2009

Keywords:
Solid oxide fuel cell
Elementary reaction kinetic model
Heterogeneous chemistry
Electrochemistry
Syngas
Anode-supported

ABSTRACT

In this paper, a detailed one-dimension transient elementary reaction kinetic model of an anode-supported solid oxide fuel cell (SOFC) operating with syngas based on button cell geometry is developed. The model, which incorporates anodic elementary heterogeneous reactions, electrochemical kinetics, electrodes microstructure and complex transport phenomena (momentum, mass and charge transport) in positive electrode|electrolyte|negative electrode (PEN), is validated with experimental performance for various syngas compositions at 750, 800 and 850 °C. The comparisons show that the simulation results agree reasonably well with the experimental data. Then the model is applied to analyze the effects of temperature and operation voltage on polarizations in each component of PEN, electronic current density in both electrodes and species concentrations distributions in anode. The numerical results of carbon deposition simulation indicate that higher temperature and lower operation voltage are helpful to reduce the possibility of carbon deposition on Ni surfaces by Bouduard reactions. Furthermore, a sensitivity analysis of cell performance on syngas composition is performed for the typical syngas from entrained-flow coal gasifier and natural methane thermochemical reforming processes. The cell performance increases with the increasing of effective compositions (e.g. H_2 and CO) in syngas and the large N_2 content introduced by using air as oxidant leads to significant deterioration of performance.

1. Introduction

Solid oxide fuel cells (SOFCs) can convert the chemical energy of fuel into electricity directly. With the rising fuel prices and stricter emission requirement, SOFCs have been widely recognized as a promising technology in the near future. In principle, besides hydrogen, a variety of hydrocarbon-based fuels, such as natural gas, biomass, coal and their derived syngas can be used directly and efficiently in SOFCs. That is because the high operation temperature offers inherently rapid electrode kinetics and the less need for high catalytic activity. However, due to the carbon deposition problems associated with pure hydrocarbon fuels, practical SOFC systems often operate on the syngas derived from them [1,2]. The hydrocarbon-based fuels can be converted by gasification or reforming to the syngas, which is essentially a mixture mainly consisted of H_2, H_2O, CO, CO_2 and N_2. Nevertheless, depending on the types of fuels and the technologies of gasification or reforming, the compositions of syngas vary widely and affect the SOFCs performances considerably [3–7]. In addition, the carbon depositions of syngas fueled SOFCs are also determined by the syngas compositions, especially the CO content. Generally, the methane-derived syngas from reforming is H_2-rich while the coal-derived syngas from gasification is CO-rich [3]. Therefore, it is necessary to clarify the SOFCs performances and electrochemical properties for various operation conditions fueled by a mixture of H_2, H_2O, CO and CO_2.

The positive electrode|electrolyte|negative electrode (PEN) is the core of SOFCs, which provides a functional material backbone for complex chemical, electrochemical and transport processes. Consequently, investigating the fundamental mechanisms and transport processes is very important for SOFCs optimization design and performance improvement. Nevertheless, it is very difficult by only experimental method to clarify internal parameters distributions and complex physical phenomena in fuel cells. Furthermore, the experimental studies on SOFCs are expensive, time-consuming and labor-intensive. Based on the above considerations, a validated mechanism model has been proved an effective method for internal phenomena comprehension, performance evaluation and design of the SOFCs.

In recent years, many SOFC models have been developed to study the fundamental mechanisms, transport phenomena and cell performances for various operation situations.

Numerous various dimensional SOFC models considering intricate interdependency among the ionic conduction, electronic

* Corresponding author. Tel.: +86 1062789955; fax: +86 1062789955.
E-mail address: cains@mail.tsinghua.edu.cn (N. Cai).

0378-7753/$ – see front matter © 2009 Elsevier B.V. All rights reserved.
doi:10.1016/j.jpowsour.2009.10.051

Nomenclature

a_i	pre-exponential factor in sticking coefficient expression
A	pre-exponential factor (in terms of cm, mol and s)
b_i	temperature exponent in sticking coefficient expression
c	concentration ($mol\,m^{-3}$)
C_{dl}	specific double-layer capacitance ($F\,m^{-2}$)
d_i	activation energy in sticking coefficient expression ($J\,mol^{-1}$)
D	diffusion coefficient ($m^2\,s^{-1}$)
E	activation energy ($kJ\,mol^{-1}$)
E_{ca}	parameter in Eq. (23) ($130\,kJ\,mol^{-1}$)
F	Faraday constant ($96{,}485\,C\,mol^{-1}$)
i_0	exchange current density ($A\,m^{-2}$)
I_F	volumetric Faradaic current ($A\,m^{-3}$)
k	reaction rate constant (in terms of m, mol and s)
K	number of species
M_k, M_j	molecular weight ($kg\,mol^{-1}$)
n	temperature exponent fraction number of electronic or ionic conductor particles
n_e	number of electrons participating in the reaction
n_t	total number of particles per unit volume
N	number of the reactions
p	pressure (Pa)
P	whole range connection probabilities of same kinds of particles
Q	source term of charge balance equations ($A\,m^{-3}$)
$\bar{r}$	average pore radius (m)
r_{el}	mean radius of the electronic conductor particle (m)
R	gas constant ($8.314\,J\,mol^{-1}\,K^{-1}$)
R_k	source term of mass balance equations ($kg\,m^{-3}\,s^{-1}$)
$\dot{s}$	molar production rate ($mol\,m^{-2}\,s^{-1}$)
S^0	initial sticking coefficient
S^{eff}	effective reaction area per unit volume ($m^2\,m^{-3}$)
S_{Ni}	Ni active surface area per unit volume ($m^2\,m^{-3}$)
S_{TPB}	TPB active area per unit volume ($m^2\,m^{-3}$)
t	time (s)
T	temperature (K)
V	voltage (V)
V_k, V_j	diffusion volume
W	molecular weight of the gas-phase species in sticking coefficient reaction ($kg\,mol^{-1}$)
x_k	molar fraction of gas-phase species k
Z	coordination number

Greek letters

α	transfer coefficient
β	tuning parameter ($\Omega^{-1}\,m^{-2}$)
γ	parameter modeling the rate constant from sticking coefficient
Γ	surface sites density ($mol\,m^{-2}$)
ε	porosity
ε_{ki}	parameter modeling the species coverage
η	overpotential (V)
θ	contact angle between the electronic and ionic conductors particles (rad)
θ_k	surface coverage of species k
μ_{ki}	parameter modeling the species coverage
ν	stoichiometric coefficient
σ	conductivity ($S\,m^{-1}$)
τ	tortuosity
χ	species symbol

Subscripts

ac	anode chamber
act	active layer
an	anode
ca	cathode
cc	cathode chamber
ec	electrochemical reactions
el	electronic conductor particles
elec	electronic
electrolyte	electrolyte
g	gas-phase species
i	reactions index
io	ionic conductor particles
ion	ionic
k	species index
Kn	Knudsen
mole	molecular
OCV	open circuit voltage
ref	reference
s	surface species
sp	support layer

Superscripts

0	parameter at equilibrium conditions
bulk	bulk phase
eff	effective
TPB	three-phase boundary

conduction, gas transport phenomena, and electrochemical processes have been reported in the literatures for pure hydrogen, syngas or methane [8–19]. In order to simplify the calculation, these published models conventionally treated the catalytic reforming and water–gas-shift reactions within anode as global kinetics reactions, or even assumed to be locally equilibrated. In fact, the adsorption–desorption reactions and water–gas-shift reactions of syngas take place heterogeneously within the anode. Consequently, it is important to understand the elementary heterogeneous chemical kinetics of syngas, especially for the anode-supported SOFCs. Hecht et al. [20] reported a multi-step heterogeneous elementary reaction mechanism for CH_4 reforming using Ni as catalyst, which was used in some SOFCs modeling and simulations [21–23]. However, the mechanism reported by Hecht et al. [20] was evaluated only at 800 °C and then Janardhanan and Deutschmann [24] developed an extended version of the mechanism evaluated for temperatures between 220 and 1700 °C. The extended mechanism was adopted to treat internal reforming of CH_4 in many SOFCs modeling literatures [25–28]. Besides the CH_4 reforming reactions, the mechanism also involves the adsorption–desorption and water–gas-shift reactions for syngas [20,24]. In these literatures [20–28], despite the consideration of heterogeneous reactions within anode, the electrochemistry was implemented using a Butler–Volmer equation based on oxygen partial pressure in both electrodes and the changes of syngas concentrations in the electrochemical reactions were directly determined by the local exchange current density.

For the simplest case of hydrogen oxidation, many possible reaction pathways and corresponding models are proposed [22,29–33]. Bieberle and Cauckler [29] developed a simplified electrochemical model which combined the charge transfer with the concentrations of surface species, oxygen interstitial and vacancy in anode for pure H_2. It is convenient for keeping the consistency of electrochemical and heterogeneous reactions in electrode. However, the electrochemical oxidation mechanism is more complex for syn-

gas [34,35]. H_2 is considered as the only electrochemically active species in some models [22,24,26,27].

Furthermore, most of the modeling studies are steady state and some transient models of SOFCs have been proposed in literatures [19,21,22,36,37]. Due to the frequently fluctuation in actual power generation, a transient model of SOFCs is needed for transient behavior prediction.

In this paper, a transient mechanistic SOFC model coupled with anodic elementary heterogeneous reactions (adsorption–desorption and water–gas-shift reactions) and electrochemical kinetics for syngas operation (mixtures of H_2, H_2O, CO, CO_2 and N_2) based on an anode-supported button cell was developed. Besides, the model takes account for the electrode microstructure and complex transport phenomena within PEN, including charge migration and species transports. Another unique advantage of this model is that it associates the electrochemical oxidation of H_2 and CO with the surface species distribution in heterogeneous reactions. Then the developed model was calibrated and validated using experimental data obtained on a button cell for various syngas compositions at 750, 800 and 850 °C. Afterwards, the model was applied for the research of fundamental mechanisms, the effects analysis of various parameters and the cell performance predictions for various typical coal-derived and methane-derived syngas. Besides, the model was also employed to study the influence of operation conditions on carbon deposition.

It should be noted that this paper preliminarily focuses on the steady state characteristics of SOFC and the model was validated using voltage–current density (*V–I*) data in experiments. However, the model developed here is convenient for the transient analysis and validation associated with transient experimental data, such as the simulations of electrochemical impedance spectra and the influences of scanning rate on *V–I* curves. Further studies on SOFC transient behavior will be summarized in our further study.

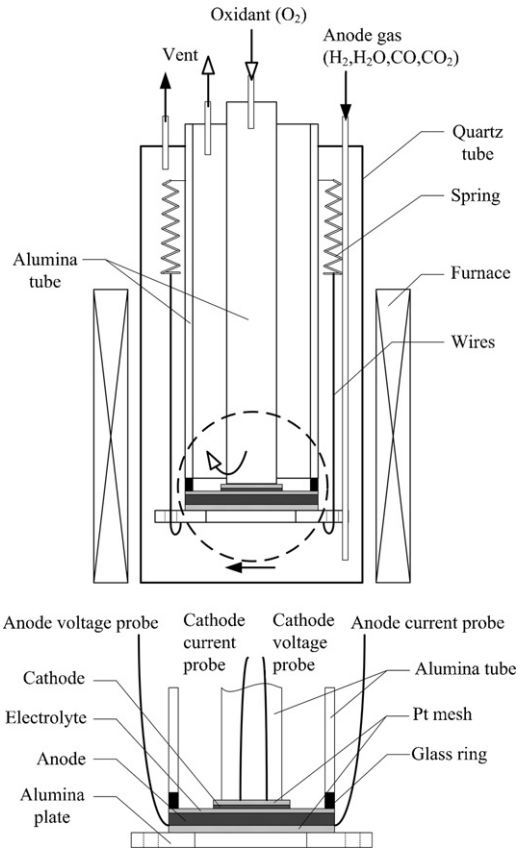

Fig. 1. Schematic of the test setup.

2. Experiment

2.1. Anode-supported button cell structure and fabrication

An anode-supported SOFC button cell made by SICCAS (Shanghai Institute of Ceramics Chinese Academy of Sciences) was employed in this study. It consists of a Ni/YSZ anode-support layer (680 μm), a Ni/ScSZ anode-active interlayer (15 μm), a ScSZ electrolyte layer (20 μm), and a lanthanum strontium manganate (LSM)/ScSZ cathode layer (15 μm) [8]. The diameter of cathode layer is 1.3 cm and diameters of other layers are all 2.6 cm.

The anode-support layer and active layer were prepared by mixing nickel oxide (NiO) powder (Inco Ltd., Canada) with 8 mol% YSZ powder (Tosoh, Japan) and with ScSZ powder ($Zr_{0.89}Sc_{0.1}Ce_{0.01}O_{2-x}$, Daiichi Kigenso Kagaku Kogyo, Japan) respectively. The powders were mixed at 50 wt% NiO and 50 wt% stabilized zirconia (YSZ or ScSZ). The electrolyte substrate was a dense film of ScSZ powder. All the ceramic powders were homogenized in a planetary mill with methyl ethyl ketone and ethanol (dispersant) to slurries. Besides, rice starch, polyvinyl butyral, polyethylene glycol and dibutyl o-phthalate were added into the anode layers slurries, which were used as pore former, blinder and plasticizer. After being vacuumed for 2 min, the ScSZ, NiO–ScSZ and NiO–YSZ slurries which were used to form electrolyte, anode-active and -support layers, were cast onto the glass plate by tape casting in sequence. After drying overnight at room temperature, the multilayer tape was detached and co-sintered at 1400 °C in air for 4 h. Then the button cells were cut out from the whole sintered plate. Therefore, the anode and electrolyte layers of all cells were fabricated in one time, which compensates the performance differences caused by cell-to-cell variations in fabrication to a certain extent. The cathode material was similarly made into paste by mixing LSM (Inframat Advanced Materials, USA) and ScSZ powders in a mass ratio of 50:50. Then, the paste was screen-printed onto the ScSZ layer of button cell and sintered at 1200 °C for 3 h to form the cathode.

Before testing, silver paste was reticulated on the anode and cathode surface by screen-printing for current collection.

2.2. Test setup

Fig. 1 shows the schematic of the test setup used for evaluating the performance of the SOFC button cell.

The button cell was located at the end of two coaxial alumina tubes and impacted by an alumina plate, which was strained by springs. The Pt mesh was used as the cathode current collector and fixed to the porous cathode with silver paste screen-printed on the surface. The oxidant flowed into the inner tube to the cathode and passed through the porous Pt mesh. Another Pt mesh was fixed to the anode-support layer with silver paste to collect anode current. The fuel was induced to the anode surrounding by an alumina tube. Due to the porous structure of Pt mesh, the anode gas reached the anode easily. For both anode and cathode, Pt wires were used as voltage and current probes. A borosilicate glass ring (SiO_2 76%, B_2O_3 15%, R_2O 6%, Al_2O_3 3%, Beijing Glass Instrument Factory, China) was used as sealant to separate the anode gas and cathode gas. All the devices were enclosed in one quartz tube and heated by a furnace to keep the operation temperature.

Before testing, pure H_2 was sent to the chamber for 1 h to fully reduce the anode at the flow rate of 50 mL min^{-1}. During the actual testing, syngas was used as fuel, which is a mixture of $H_2/H_2O/CO/CO_2$ at a given proportion; pure oxygen was used as oxidant. The flow rates of both fuel and oxygen were kept at 300 mL min^{-1}.

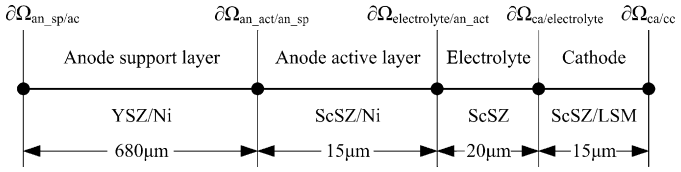

Fig. 2. Illustration of simplified 1D model geometry of SOFC button cell.

The polarization curves were measured using four-probe method with an electrochemical workstation (IM6ex, Zahner-Elektrik GmbH, Germany). Electrochemical impedance spectroscopy (EIS) was performed using amplitude of 10 mV over the frequency from 0.1 Hz to 100 kHz. The ohmic resistance of button cell was estimated from the high frequency intercept of the impedance curve. The measurements were initiated when the temperature changing 30 min later until the system was stable. After the cell tests, the microstructure of anode was characterized using mercury porosimeter.

3. Model development

3.1. Model assumptions and geometry

The model assumptions are listed as follows:

(1) All gas mixtures are considered as ideal gas.
(2) The temperature of button cell is uniform and the model is assumed isothermal. All the model parameters are evaluated at a given temperature.
(3) The convection flux and pressure gradient in the porous electrodes are ignored.
(4) The microstructures of electrodes are stable and homogeneous in operation. The carbon deposition influence to the pore structure and reaction activities in anode is disregarded. Besides, the distributions of the two conducting phases (electronic and ionic) in electrodes are assumed to be uniform.
(5) The heterogeneous and the electrochemical reactions are assumed to only take place on the Ni surface and directly at the TPB, respectively. Thus, Ni is used as catalyst and the all the active sites only exist on the Ni surface for heterogeneous reactions, which involve gas adsorption or desorption reactions and surface reactions.
(6) All surface species are considered to be uncharged and the charge transfer reactions (electrochemical reactions) are assumed to take place in one step.
(7) For anode heterogeneous reactions, mean field approximation is used, i.e. the surface adsorbates are assumed to be uniformly distributed over the catalyst surface.
(8) The transport of surface species over microscopic distances caused by surface diffusion is assumed to be negligible.

The button cell used in this work has a smaller cathode compared with anode and electrolyte. The special geometry causes the significant non-uniform distributions of current and gas concentrations in anode in radial direction [9,10]. Fortunately, at the center of button cell where covers with cathode, all the parameters are relatively uniform. In this work, the focuses are concentrated on parameters distribution in the thickness direction and the radial non-uniformity is neglected. In order to reduce calculation complication, the one-dimensional (1D) SOFC geometry is adopted as that illustrated in Fig. 2. In this figure, the model structures, calculation domains and boundaries are labeled schematically, which will be described later.

As described in cell fabrication, the ionic conductors of anode-support layer and anode-active layer are YSZ and ScSZ, respectively. The anode-active layer has a higher ionic conductivity and better thermal compatibility than anode-support layer. However, it should be noted that the electrochemical reactions maybe take place not only in anode-active layer but also in anode-support layer, especially for the thin anode-active layer. Therefore, the governing equations of charge and mass balance for anode-support layer are the same as those for the anode-support layer, although some parameters may be different. Besides, due to the similar oxygen ionic conduction mechanisms of YSZ and ScSZ, the one step electrochemical reactions are the same for anode-support and -active layers. In addition, the electron conductors of anode-support layer and anode-active layer are both Ni, which is assumed to be the only catalyst of heterogeneous reactions. Thus, the same heterogeneous reaction kinetic parameters are used for both layers.

Within the above assumptions and simplified model geometry, a 1D SOFC model is formulated considering anodic heterogeneous chemistry, electrochemistry, charge and mass balance, as described in the following sections.

3.2. Governing equations

3.2.1. Anode heterogeneous chemistry

Within a syngas fueled SOFC, a mixture of H_2, H_2O, CO, CO_2 exists and water–gas-shift reaction proceeds in the anode, where it is necessary to consider the heterogeneous chemistry and varied species distributions. In contrast, there is no significant heterogeneous reaction in cathode. In this work, anodic syngas heterogeneous chemistry based on molecular behavior at the catalytic surface is developed. In Ni–YSZ anode, Ni is an effective catalyst for surface elementary reactions, especially for the hydrocarbon fueled SOFC. Hecht et al. [20] reported a multi-step heterogeneous reaction mechanism for CH_4 using Ni as catalyst. The mechanism was evaluated only at 800 °C and then Janardhanan and Deutschmann [24] developed an extended version of the mechanism evaluated for temperatures between 220 and 1700 °C.

The elementary mechanism reflects all the characteristics of reforming, water–gas-shift and Bouduard reactions. There is no significant internal reforming reaction and hydrocarbon species in anode for syngas fueled SOFC. A simplified heterogeneous mechanism from Janardhanan and Deutschmann [24] is used in this study. The simplified mechanism, which consists of 20 irreversible reactions and involves 5 gaseous species and 8 surface-adsorbed species, is listed in Table 1 (the complete mechanism can be downloaded from www.detchem.com/mechanism).

Using a mean field approximation, the surface adsorbates are assumed to be uniformly distributed over the catalyst surface. Then the species molar production rates depend on the gaseous species concentrations or surface species concentrations, which sometimes expressed as coverage θ_k. The coverage θ_k is the fraction of the surface sites covered by the adsorbed species k to the all active sites on catalyst surface. It is assumed that the total number of surface active sites is conserved and the saturation sorbent capacity is described by the maximum surface sites density Γ [38]. Furthermore, the uncovered surface of catalyst Ni is also can be treated as a surface species. Then, the heterogeneous reactions, including gaseous adsorption–desorption reactions and surface reactions can be written in the same form [38]

$$\sum_{k=1}^{K_g+K_s} \nu'_k \chi_k \Rightarrow \sum_{k=1}^{K_g+K_s} \nu''_k \chi_k \quad (1)$$

where χ_k is the kth species in the reaction, ν'_k and ν''_k are the stoichiometric coefficients of reactants and products, K_g and K_s is the number of gaseous species and surface species, respectively. The net molar production rate $\dot{s}_k$ of a gaseous species or a surface species

Table 1
Heterogeneous reactions mechanism on Ni-based catalysts.

	Reaction	A[a]	n[a]	E[a]
1	$H_2 + Ni(s) + Ni(s) \rightarrow H(s) + H(s)$	1.000×10^{-02}[b]	0.0	0.00
2	$O_2 + Ni(s) + Ni(s) \rightarrow O(s) + O(s)$	1.000×10^{-02}[b]	0.0	0.00
3	$H_2O + Ni(s) \rightarrow H_2O(s)$	0.100×10^{-00}[b]	0.0	0.00
4	$CO_2 + Ni(s) \rightarrow CO_2(s)$	1.000×10^{-05}[b]	0.0	0.00
5	$CO + Ni(s) \rightarrow CO(s)$	5.000×10^{-01}[b]	0.0	0.00
6	$H(s) + H(s) \rightarrow Ni(s) + Ni(s) + H_2$	$2.545 \times 10^{+19}$	0.0	81.21
7	$O(s) + O(s) \rightarrow Ni(s) + Ni(s) + O_2$	$4.283 \times 10^{+23}$	0.0	474.95
8	$H_2O(s) \rightarrow H_2O + Ni(s)$	$3.732 \times 10^{+12}$	0.0	60.79
9	$CO_2(s) \rightarrow CO_2 + Ni(s)$	$6.447 \times 10^{+07}$	0.0	25.98
10	$CO(s) \rightarrow CO + Ni(s)$	$3.563 \times 10^{+11}$ $\theta_{CO(s)}$	0.0	111.27 −50.00[c]
11	$H(s) + O(s) \rightarrow OH(s) + Ni(s)$	$5.000 \times 10^{+22}$	0.0	97.90
12	$OH(s) + Ni(s) \rightarrow H(s) + O(s)$	$1.781 \times 10^{+21}$	0.0	36.09
13	$H(s) + OH(s) \rightarrow H_2O(s) + Ni(s)$	$3.000 \times 10^{+20}$	0.0	42.70
14	$H_2O(s) + Ni(s) \rightarrow H(s) + OH(s)$	$2.271 \times 10^{+21}$	0.0	91.76
15	$OH(s) + OH(s) \rightarrow H_2O(s) + O(s)$	$3.000 \times 10^{+21}$	0.0	100.00
16	$H_2O(s) + O(s) \rightarrow OH(s) + OH(s)$	$6.373 \times 10^{+23}$	0.0	210.86
17	$C(s) + O(s) \rightarrow CO(s) + Ni(s)$	$5.200 \times 10^{+23}$	0.0	148.10
18	$CO(s) + Ni(s) \rightarrow C(s) + O(s)$	$1.354 \times 10^{+22}$ $\theta_{CO(s)}$	−3.0	116.12 −50.00[c]
19	$CO(s) + O(s) \rightarrow CO_2(s) + Ni(s)$	$2.000 \times 10^{+19}$ $\theta_{CO(s)}$	0.0	123.60 −50.00[c]
20	$CO_2(s) + Ni(s) \rightarrow CO(s) + O(s)$	$4.653 \times 10^{+23}$	−1.0	89.32

[a] Arrhenius parameters for the rate constant written in the form: $k = AT^n \exp(-E/RT)$. The units of A are given in terms of moles, cm, and s. E is in kJ mol^{-1}.
[b] Sticking coefficient.
[c] Coverage dependent activation energy.

in a heterogeneous reaction can be written as:

$$\dot{s}_k = \sum_{i=1}^{N} (\nu''_{ki} - \nu'_{ki}) k_i \prod_{k=1}^{K_g+K_s} c_k^{\nu'_{ki}} \quad (2)$$

where N is the total number of reactions and c_k is the concentration of the kth species. For all the surface reactions and desorption reactions, the reaction rate constant k_i for the ith reaction is presented in the general modification Arrhenius form [24]:

$$k_i = A_i T^{n_i} \exp\left(-\frac{E_i}{RT}\right) \prod_{k=1}^{K_g+K_s} \theta_k^{\mu_{ki}} \exp\left(-\frac{\varepsilon_{ki}\theta_k}{RT}\right) \quad (3)$$

where A_i, n_i and E_i are the Arrhenius number which are listed in Table 1, R is the gas constant, T is the reaction temperature, μ_{ki} and ε_{ki} are the parameters describe the species coverage dependency of rate constants for species k and reaction i. Here for most of the reactions, which are independent of species coverage, μ_{ki} and ε_{ki} are both 0 and the effects of species dependency are ignored. But for the reactions (10), (18) and (19), the reaction rate constants of which relay on the CO(s) coverage $\theta_{CO(s)}$. Then, μ_{ki} is 0 and ε_{ki} for corresponding reactions are listed in Table 1.

For absorption reactions, the rate constants are expressed in sticking coefficient form [38]

$$k_i = \frac{S_i^0}{\Gamma^\gamma} \sqrt{\frac{RT}{2\pi W}} \quad (4)$$

where S_i^0 is the initial sticking coefficient, W is the molecular weight of the gas-phase species, and

$$\gamma = \sum_{k}^{K_s} \nu'_{ki} \quad (5)$$

sticking coefficient S_i^0 is temperature dependent and expressed as

$$S_i^0 = a_i T^{b_i} \exp\left(-\frac{d_i}{RT}\right) \quad (6)$$

where a_i and b_i are dimensionless parameters and d_i has the compatible units with RT. These parameters can be treated as Arrhenius number which also listed in Table 1.

3.2.2. Anode electrochemistry

Electrochemical reactions take place with electric current transport and convert chemical energy into electrical energy. All electrochemical reactions of fuel cell exist in the two electrodes separated by the electrolyte. Here the electrochemistry elementary reactions in anode are analyzed in detail and those in cathode are neglected. However, the electrochemical processes in a fuel cell are quite complex in nature. The elementary reactions and charge transfer at the TPB are the predominant concern and still under research. For the simplest case of hydrogen oxidation, many possible reaction pathways and corresponding models are proposed [22,29–33]. The reaction system mainly consists of gaseous species adsorption–desorption reactions, surface reactions and interface electrochemical reactions at TPB. According to the model assumptions, all the active sites only exist on the Ni surface. In order to keep the consistency of electrochemical and heterogeneous reactions, the interface electrochemical reaction at TPB can be expressed as [29]

$$O_O^x + Ni(s) \xrightarrow{k_{ec}} O(s) + V_O^{\bullet\bullet} + 2e^- \quad (7)$$

$$O(s) + V_O^{\bullet\bullet} + 2e^- \xrightarrow{k_{-ec}} O_O^x + Ni(s) \quad (8)$$

where O_O^x denotes an oxygen interstitial and $V_O^{\bullet\bullet}$ an oxygen vacancy in the ionic conductor, while e^- denotes the electron in the electronic conductor Ni. k_{ec} and k_{-ec} are the forward and reverse electrochemical reaction rates, respectively.

Nevertheless, it is well known that H_2 and CO both participate in charge transfer chemistry and some possible reaction pathways of the mixture of H_2 and CO are proposed [34,35]. It is reported that H_2 oxidation kinetics dominates over CO oxidation [34] and the conversion rate of CO in water–gas-shift reaction exceeds that in the electrochemical oxidation [35]. So H_2 is consid-

ered as the only electrochemically active species in some models [22,24,26,27]. Fortunately, the interface electrochemical reactions here do not involve the species composed of C or H and also can be used for syngas fueled system. The effects of H_2 and CO to the SOFC performances are reflected in the heterogeneous reactions.

According to the Faraday's law, the electrochemical reactions associate the exchange current between ionic and electronic conductors in anode together with the concentrations of species as

$$I_F = 2FS_{TPB}(k_{ec}c_{O_O^x}c_{Ni(s)} - k_{-ec}c_{O(s)}c_{V_O^{\bullet\bullet}}) \quad (9)$$

where I_F is the volumetric Faradaic current, F is the Faraday constant, S_{TPB} is the TPB active area per unit volume. $c_{O(s)}$ and $c_{Ni(s)}$ denote the surface concentrations of the species O adsorbed on the Ni surface and the free surface sites, respectively. $c_{O_O^x}$ and $c_{V_O^{\bullet\bullet}}$ denote the volumetric concentrations of oxygen interstitial and oxygen vacancy in the ionic conductor.

The forward and reverse electrochemical reaction rates have been formulated by Bieberle and Cauckler [29] using electrochemical impedance spectrums method as follows

$$k_{ec} = k_{ec}^0 \exp\left(-2\alpha\frac{F}{RT}\eta_{an}\right) \quad (10)$$

$$k_{-ec} = k_{-ec}^0 \exp\left(-2(1-\alpha)\frac{F}{RT}\eta_{an}\right) \quad (11)$$

where α is the charge transfer coefficient and η_{an} is the anodic overpotential which will be described later. The parameters k_{ec}^0 and k_{-ec}^0 can be calculated as

$$k_{ec}^0 = \frac{i_0}{FS_{TPB}c_{O_O^x}^0 c_{Ni(s)}^0} \quad (12)$$

$$k_{-ec}^0 = \frac{i_0}{FS_{TPB}c_{O(s)}^0 c_{V_O^{\bullet\bullet}}^0} \quad (13)$$

where k_{ec}^0, k_{-ec}^0, $c_{O_O^x}^0$, $c_{Ni(s)}^0$, $c_{O(s)}^0$, $c_{V_O^{\bullet\bullet}}^0$ have their usual meaning under equilibrium conditions, when no net current is observed at the TPB. i_0 is the exchange current density at equilibrium conditions.

If the oxygen interstitial and oxygen vacancy are treated as normal volumetric species, the electrochemical and heterogeneous reaction rates can be expressed in the general form

$$\dot{s}_k = \sum_{i=1}^{N+2}(\nu_{ki}'' - \nu_{ki}')k_i \prod_{k=1}^{K_g+K_s+2} c_k^{\nu_{ki}'} \quad (14)$$

where $N+2$ denotes the total number of the heterogeneous and the electrochemical reactions, and K_g+K_s+2 denotes the total number of gaseous species, surface species, oxygen interstitial and oxygen vacancy.

3.2.3. Effective reaction areas

The heterogeneous reaction rates and electrochemical reaction rates also relate to the concentrations of surface species. Consequently, in order to obtain the volumetric reaction rates in the anode, the effective reaction areas for all kinds of reactions per unit volume are needed. According to the model assumptions, the heterogeneous reactions and electrochemical reactions only take place at the Ni surface and TPB, respectively. Therefore, the Ni active surface area per unit volume S_{Ni} and TPB active area per unit volume S_{TPB} in anode need to be determined.

The calculation of parameter S_{TPB} is a research focus in SOFCs modeling and simulations [39–41]. According to the particle coordination number theory in binary random packing of spheres and the percolation theory, S_{TPB} can be formulated as

$$S_{TPB} = \frac{\pi \sin^2\theta r_{el}^2 n_t n_{el} n_{io} Z_{el} Z_{io} P_{el} P_{io}}{Z} \quad (15)$$

where Z is the mean coordination number, r_{el} is the mean radius of the electronic conductor particle, θ is the contact angle between the electronic and ionic conductors particles, n_t is the total number of particles per unit volume, n_{el} and n_{io} are the fraction number of electronic and ionic conductor particles, Z_{el} and Z_{io} are the coordination numbers of electron and ion conductor particles, and P_{el} and P_{io} are the whole range connection probabilities of the same kinds of particles. Here S_{TPB} is treated as the contact area of different kinds of particles. The detailed model description and parameters calculation can be found in the literature [40,41].

Enlightened by the calculation of S_{TPB}, S_{Ni} can be treated as the total Ni particles surface area minus the contact surface area around the Ni particles per unit volume. The contact surface area consists of two parts, the contact surface area between Ni and YSZ particles and that between two Ni particles. It is assumed that the Ni particles and YSZ particles are the same in the sizes and fraction number. Both the contact angles between Ni particles themselves and two different particles are set as $(\pi/12)$ rad in this paper. Then, the effective Ni surface area per unit volume can be formulated as

$$S_{Ni} = \pi r_{el}^2 n_t n_{el}\left(4 - \frac{\sin^2\theta n_{io} Z_{el} Z_{io}}{Z} - \frac{\sin^2\theta n_{el} Z_{el} Z_{el}}{Z}\right) \quad (16)$$

where the three terms on the right of equation denote the total Ni particles surface area, the contact surface area between Ni and YSZ particles and that between two Ni particles per unit volume, respectively. It is noted that the calculation of S_{Ni} does not involve the connection probabilities of the same kinds of particles, which is different from the S_{TPB}. That is because the transport of current is not needed in heterogeneous reactions and all the Ni particle surface can be used as catalyst.

3.2.4. Charge balance

Some transient models of SOFC have been proposed in literatures [19,21,22,36,37]. Shi et al. [36] developed a transient physical model of SOFC, which is used in this paper to describe the charge balance. Only the model formulations, as well as differences between the present model and the model in [36] are presented here.

For electrodes, the charge balance equations considering the transient effects of double-layer capacitance are formulated as

$$\frac{\partial[C_{dl}S_{TPB}(V_i - V_j)]}{\partial t} + \nabla(-\sigma^{eff}\nabla V_i) = Q \quad (17)$$

where t is time, C_{dl} is the specific interface double-layer capacitance between electronic and ionic conductor phase, Q is the current source, V_i and V_j are the electric potential of either ionic or electron conductor phases, σ^{eff} is the corresponding conductor phase effective conductivity.

The charge balance equations have respective expressions for two electrodes and electrolyte. The cathode ionic charge and electronic charge equations can be formulated as follows

$$\frac{\partial(C_{dl,ca}S_{TPB,ca}(V_{ion,ca} - V_{elec,ca}))}{\partial t} + \nabla\cdot(-\sigma_{ion,ca}^{eff}\nabla V_{ion,ca}) = Q_{ion,ca}$$
$$= -i_{0,ca}S_{TPB,ca}\left\{\frac{c_{O_2}^{TPB}}{c_{O_2}^{bulk}}\exp\left[\frac{\alpha n_e F\eta_{ca}}{RT}\right] - \exp\left[-\frac{(1-\alpha)n_e F\eta_{ca}}{RT}\right]\right\} \quad (18)$$

$$\frac{\partial(C_{dl,ca}S_{TPB,ca}(V_{elec,ca} - V_{ion,ca}))}{\partial t} + \nabla\cdot(-\sigma_{elec,ca}^{eff}\nabla V_{elec,ca}) = Q_{elec,ca}$$
$$= -Q_{ion,ca} \quad (19)$$

where $c_{O_2}^{TPB}$ and $c_{O_2}^{bulk}$ are the cathode oxygen concentrations at the TPB and in the bulk, respectively, α is the charge transfer coefficient, n_e is the number of electrons participating in the reaction, and η_{ca} is the cathode local overpotential, which defined as [39]

$$\eta_{ca} = V_{elec,ca} - V_{ion,ca} - V_{ref,ca} \quad (20)$$

where $V_{ref,ca}$ is the cathode local relative potential difference between the electronic conductors at a reference state. Similar to the cathode local overpotential, the anode local overpotential η_{an} used in Section 3.2.2 is defined as

$$\eta_{an} = V_{elec,an} - V_{ion,an} - V_{ref,an} \quad (21)$$

By setting anode reference potential $V_{ref,an}$ to zero, the cathode reference potential $V_{ref,ca}$ equals to the actual cell open circuit voltage (OCV), V_{OCV} [36]. Generally, the calculation of V_{OCV} for syngas is based on the H_2 oxidation mechanism [24], in which H_2 is assumed the only electrochemically active species and the Nernst equation of H_2 is used to predict the OCV. The simplification neglects the simultaneous electrochemical oxidation of H_2 and CO and brings in deviation to the predictions. Essentially, the SOFC is a concentration cell of O_2 and the OCV can be determined by Nernst equation as [42]

$$V_{OCV} = \frac{RT}{n_e F} \ln\left(\frac{p_{ca}^{O_2}}{p_{an}^{O_2}}\right) \quad (22)$$

where $p_{ca}^{O_2}$ and $p_{an}^{O_2}$ are the equilibrium oxygen partial pressures in cathode and anode, respectively. Here $p_{an}^{O_2}$ is determined by the heterogeneous reactions mechanism in Section 3.2.1 and the composition of fuel in anode.

The cathode exchange current density $i_{0,ca}$ is expressed as [39]

$$i_{0,ca} = \frac{\beta RT}{4F} \exp\left(-\frac{E_{ca}}{RT}\right) (p_{ca}^{O_2})^{0.25} \quad (23)$$

where E_{ca} is 130 kJ mol^{-1}, and β is treated as an adjustable parameter to fit the experimental data.

The anode ionic charge and electronic charge equations can be formulated as

$$\frac{\partial(C_{dl,an} S_{TPB,an}(V_{ion,an} - V_{elec,an}))}{\partial t} + \nabla \cdot (-\sigma_{ion,an}^{eff} \nabla V_{ion,an}) = Q_{ion,an} \quad (24)$$

$$\frac{\partial(C_{dl,an} S_{TPB,an}(V_{elec,an} - V_{ion,an}))}{\partial t} + \nabla \cdot (-\sigma_{elec,an}^{eff} \nabla V_{elec,an}) = Q_{elec,an} = -Q_{ion,an} \quad (25)$$

The ionic current source in anode $Q_{ion,an}$ equals to the volumetric Faradaic current I_F defined in Section 3.2.2.

There are no double-layer capacitance effects and current sources or sinks in electrolyte. Consequently, the electrolyte charge balance equation can be briefly expressed as

$$\nabla \cdot (-\sigma_{ion,electrolyte}^{eff} \nabla V_{ion,electrolyte}) = 0 \quad (26)$$

where $\sigma_{ion,electrolyte}^{eff}$ is the effective ionic conductivity of electrolyte and $V_{ion,electrolyte}$ is the ionic potential in electrolyte.

3.2.5. Mass balance

Gas transport in the porous electrodes is very important for fuel cell reactions and performance. Generally, either the extended Fick's model (EFM) or the dusty-gas model (DGM) is used to describe the gaseous mass transport in porous media [43]. Both the EFM and the DGM are the mass balance equations considering Knudsen diffusion, molecular diffusion and the mass transport of a finite pressure gradient. It is generally agreed that DGM is superior to EFM to predict the fluxes inside porous media [44] and used in many SOFC models [8,10,25]. However, EFM allows explicit analytical expressions derived for fluxes and reduces the computational complexity, which also used in SOFC gas transport modeling [41]. Suwanwarangkul et al. [45] established SOFC models based on EFM and DGM for anode mass transport and compared the differences of simulation results.

Here the EFM is used to describe the mass transfer in porous electrodes and the effect of finite pressure gradient is neglected. Consequently, the EFM equation in porous electrode can be formulated as

$$\varepsilon \frac{\partial c_{k,g}}{\partial t} + \nabla(-D_k^{eff} \nabla c_{k,g}) = R_{k,g} \quad (27)$$

where ε is the porosity of electrode, $c_{k,g}$ is the gas molar concentration, $R_{k,g}$ is the mass balance source term of gaseous specie inside the porous medium, and D_k^{eff} is the effective diffusivity of gaseous species k. Considering the molecular diffusion and Knudsen diffusion, which are dominant for large pore sizes and significant when pore sizes smaller than molecular mean-free path, respectively, the effective diffusivity D_k^{eff} can be formulated as

$$D_k^{eff} = \left(\frac{1}{D_{k,mole}^{eff}} + \frac{1}{D_{k,Kn}^{eff}}\right)^{-1} \quad (28)$$

where $D_{k,mole}^{eff}$ and $D_{k,Kn}^{eff}$ is the effective molecular diffusion coefficient and effective Knudsen diffusion coefficient, respectively. For multi-components gas, the effective molecular diffusion coefficient can be calculated as [44]

$$D_{k,mole}^{eff} = \left[\frac{1 - x_k}{\sum_{j=1, j\neq k}^{n} (x_j / D_{k,j}^{eff})}\right] \quad (29)$$

where x_k and x_j are the fractions of molar concentrations of gaseous species k and j, and $D_{k,j}^{eff}$ is the effective binary molecular diffusion coefficient. The effective molecular diffusion coefficient of kth gaseous species is restricted to the situation wherein the species k diffuses in a mixture of stagnant and non-transferring species. Considering the porous material property, effective binary molecular diffusion coefficient $D_{k,j}^{eff}$ and effective Knudsen diffusion coefficient $D_{k,Kn}^{eff}$ can be calculated as

$$D_{k,j}^{eff} = \frac{\varepsilon}{\tau} D_{k,j} = \frac{0.00101 \varepsilon T^{1.75} ((1/M_k) + (1/M_j))^{1/2}}{\tau p [V_k^{1/3} + V_j^{1/3}]^2} \quad (30)$$

$$D_{k,Kn}^{eff} = \frac{\varepsilon}{\tau} D_{k,Kn} = \frac{4}{3} \frac{\varepsilon}{\tau} \bar{r} \sqrt{\frac{8RT}{\pi M_k}} \quad (31)$$

where τ is the tortuosity factor, V is the diffusion volume, M is the molecular weight, p is the total pressure of gas, and $\bar{r}$ denotes the average pore radius.

In the cathode, the relationship between the mass balance source term and the current source term can be determined by Faraday's law as

$$R_{O_2} = \frac{Q_{elec,ca}}{4F} \quad (32)$$

The reaction rate of nitrogen is zero and the molar fraction can be determined by

$$x_{N_2} = 1 - x_{O_2} \quad (33)$$

Within the anode, the pore size is comparable to the molecular mean-free-path length and there is very little chance for gas–gas collisions [20]. Consequently, the gas-phase reactions are neglected

Table 2
Boundary conditions.

Boundary	Ionic charge	Electronic charge	Mass balance
$\partial\Omega_{an\_sp/ac}$	Insulation	V_{an}	$c_{g,an}$ for gaseous species Insulation for surface species
$\partial\Omega_{an\_act/an\_sp}$	Continuity	Continuity	Continuity
$\partial\Omega_{electrolyte/an\_act}$	Continuity	Insulation	Insulation
$\partial\Omega_{ca/electrolyte}$	Continuity	Insulation	Insulation
$\partial\Omega_{ca/cc}$	Insulation	V_{ca}	$c_{g,ca}$

and only the heterogeneous reactions and electrochemical reaction is considered in the anode.

For surface species mass balance in the anode, the transport caused by surface diffusion is neglected and there is no conduction term in the mass balance equation, consequently. However, in order to obtain the surface species concentration distributions in the anode and reduce the complexity of calculation convergence, the mass balance equation of surface species is formulated similar to the gaseous species

$$\frac{\partial c_{k,s}}{\partial t} + \nabla(-D_s \nabla c_{k,s}) = R_{k,s} \tag{34}$$

where $c_{k,s}$ is the molar concentration of surface specie, $R_{k,s}$ is the mass balance source term of surface specie, D_s is a parameter compatible to the diffusion coefficient and should be small enough. It is found that if D_s is smaller than 1E−6, there is no obvious differences in the SOFC performance and the anodic concentration distributions of surface species.

Not similar to the cathode, the mass balance source terms in the anode are determined by kinetic reaction rates per unit volume of heterogeneous and electrochemical reactions. For both gaseous and surface species in the anode, the source terms $R_{k,g}$ and $R_{k,s}$ can be expressed in the same form

$$R_k = S^{\text{eff}} \cdot \dot{s}_k = S^{\text{eff}} \cdot \sum_{i=1}^{N+2} (\nu''_{ki} - \nu'_{ki}) k_i \prod_{k=1}^{K_g+K_s+2} c_k^{\nu'_{ki}} \tag{35}$$

where S^{eff} is the effective reaction area per unit volume, which equals to S_{Ni} or S_{TPB} for heterogeneous and electrochemical reactions, respectively.

To simplify the calculations, the concentrations of oxygen interstitial and oxygen vacancy are treated as constant. In fact, the concentrations of oxygen interstitial and oxygen vacancy in ionic conductor are several orders of magnitude larger than the concentrations of gaseous and surface species and the simplification is reasonable.

3.3. Boundary conditions

According to the operation situations and model simplifications, the boundary conditions of charge and mass balances partial differential equations are specified in Table 2. The boundaries of model geometry are labeled in Fig. 2, schematically.

The boundary conditions "Insulation" and "Continuity" mean that the partial derivative is zero and the flux is continuous of the variables at the boundary, respectively. $c_{g,an}$ and $c_{g,ca}$ in the table are the molar fractions of gaseous species in the anode and cathode. At the interface of anode and anode chamber, the boundary conditions for surface species are "Insulation", which is different from gaseous species. That is because there is no surface species out of the anode. The difference between V_{an} and V_{ca} is the cell operation voltage in the calculation. Here V_{an} is set to zero.

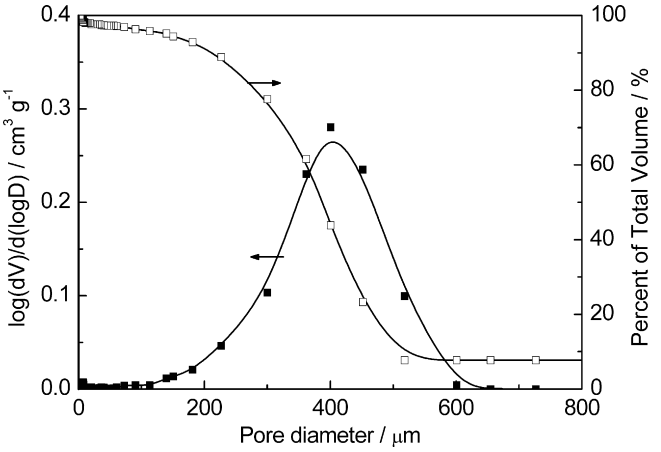

Fig. 3. Pore diameter distribution of anode-support layer characterized by mercury porosimeter.

3.4. Model parameters

Besides the parameters given in model equations descriptions, some other parameters are needed to solve the SOFC model. Those parameters are: pore structure parameters in porous electrodes, ionic or electronic conductivities of all layers and some other calculation parameters.

The pore structure of the anode-support layer was characterized using mercury porosimeter, which is shown in Fig. 3. The mean pore diameter, porosity and total pore area were found to be 0.387 μm, 0.335 and 8.54×10^6 m^2 m^{-3}, respectively. To simplify the calculation, the mean particle diameters of the two conductors are assumed to be the same and equal to the mean pore diameter [46]. With this assumption and the expressions of effective reaction areas, the calculated values of S_{TPB} and S_{Ni} in the anode-support layer are 2.22×10^5 and 3.97×10^6 m^2 m^{-3}, respectively. The calculated value of S_{Ni} is nearly a half of the experimental total pore area, which confirmed the calculation correction indirectly.

It is very difficult to characterize the pore structures of anode-active layer and cathode layer by experiment since they are very thin and hard to be separated from the button cell. Shi et al. [8] used image processing software to determine the pore size

Table 3
Pore structure parameters in porous electrode.

Cell layer	Porosity	Mean pore diameter (μm)	S_{TPB} (m^2 m^{-3})	S_{Ni} (m^2 m^{-3})
Anode-support layer	0.335	0.193	2.22×10^5	3.97×10^6
Anode-active layer	0.335	0.129	3.33×10^5	5.96×10^6
Cathode layer	0.335	0.161	2.66×10^5	–

Table 4
Properties and parameters for model calculation.

Property and parameter	Value or expression	Unit
Ionic conductivity (σ_{ion})		
ScSZ	6.92E4 exp(−9681/T) [8]	S m^{-1}
YSZ	3.34E4 exp(−10,300/T) [47]	S m^{-1}
Electronic conductivity (σ_{elec})		
LSM	4.2E7/T exp(−1150/T) [47]	S m^{-1}
Ni	3.27E6−1065.3T [48]	S m^{-1}
Equivalent ionic conductivity of electrolyte layer ($\sigma_{electrolyte}$)	$-3.622E{-}5T^2 + 0.083T - 46.343$[a]	S m^{-1}
Concentration of oxygen interstitial in the YSZ ($c_{O_O^x}$)	4.45E4 [49]	mol m^{-3}
Concentration of oxygen interstitial in the YSZ ($c_{v_O^{\bullet\bullet}}$)	4.65E3 [49]	mol m^{-3}
Maximum surface sites density (Γ)	2.6E5 [20]	mol m^{-2}
Faraday current (i_0)	420 [29]	A m^{-2}
Cathode tortuosity (τ_{ca})	3.0 [36]	
Interface double-layer capacitance ($C_{dl,an}$, $C_{dl,ca}$)	27 [36]	F m^{-2}

[a] Curve fitting according to the experimental data.

and porosity of each layer compared to anode-support layer from SEM image based on quantitative stereology. It is found that the mean pore size in anode-support layer is nearly 1.2 and 1.5 times of that in cathode layer and anode-active layer, but the porosities of all three layers are almost the same. Table 3 lists the porosity, mean pore diameter, S_{TPB} and S_{Ni} in each layer.

Table 4 lists the material conductivities and some other calculation parameters. The equivalent ionic conductivity of electrolyte layer (i.e. when the whole conductivity of the cell is reduced to that of the electrolyte layer) was determined by the ohmic resistance of the whole cell, which was estimated from the high frequency intercept of the impedance curves at open circuit state. According to the evaluated conductivities at 750, 800 and 850 °C, the equivalent ionic conductivity of electrolyte layer was given by quadratic curve fitting as a function of temperature. The interface double-layer capacitances between electronic and ionic conductor phase are specified the same for both anode layers, since the anode-active layer is very thin compared with anode-support layer. In addition, all the kinetic parameters for heterogeneous reactions and electrochemical reactions are also the same for both anode layers, which have been explained in Sections 3.2 and 3.3 in detail.

3.5. Solution method

The calculations of model were performed using the finite element commercial software COMSOL MULTIPHYSICS®, Version 3.2.

The button cell performance was calculated at a given cell voltage V_{ca}. In order to approach the actual experimental testing, a linear scanning V_{ca} at rate of 10 mV s^{-1} was used in calculation, which was the same as polarization curve measurement. For 1D SOFC model, the average current density at a given cell voltage was treated as that in electrolyte. Then, with the scanning of cell voltage, a complete polarization curve was generated.

Table 5
Gases compositions of the fuels used in this study.

Temperature (°C)	Fuel no.	Composition			
		H_2 (%)	H_2O (%)	CO (%)	CO_2 (%)
800	FI-1	100	0	0	0
	FI-2	96.9	3.07		
	FII-1	80	0	20	0
	FII-2	60		40	
	FII-3	40		60	
	FIII-1	80	0	0	20
	FIII-2	60			40
	FIII-3	40			60
	FIII-4	20			80
	FIV-1	0	0	80	20
	FIV-2			60	40
	FIV-3			40	60
	FIV-4			20	80
	FV-1	38.8	3.07	38.8	19.4
	FV-2	58.2		19.4	19.4
	FV-3	19.4		58.2	19.4
	FV-4	19.4		38.8	38.8
	FV-5	19.4		19.4	58.2
750/850	FI-1	100	0	0	0
	FI-2	96.9	3.07		
	FIV-1	0	0	80	20
	FIV-5			50	50
	FIV-4			20	80
	FV-2	58.2	3.07	19.4	19.4
	FV-3	19.4		58.2	19.4
	FV-4	19.4		38.8	38.8
	FV-5	19.4		19.4	58.2

4. Experiment results and model validation

4.1. Experimental and operation conditions

The button cell performances were measured experimentally at three temperatures (750/800/850 °C). In order to improve the model validation for syngas, the experiments were extended to various fuel compositions in this study, which are listed in Table 5. The fuel was saturated at 25 °C for water content cases. In addition, oxygen was used as oxidant. The flow rates of fuel and oxidant were both kept at 300 mL min^{-1} for all experiments.

4.2. Model calibration

Ideally, all the model parameters should be determined from literatures or experiments data. Unfortunately, some parameters cannot be determined directly and must be tuned in a reasonable range to fit the experimental data during the calibration step. The model parameters are tuned according to the FIII and FIV cases at 800 °C, which are summarized in Table 6.

The anode tortuosity, which affects the diffusion transport rate through the porous anode, is tuned to 5.5 here for all the gas in anode except H_2. It is found that the diffusion transport rate of H_2 is overestimated in model calibration and revised by an individual anode tortuosity of 7.9. The tortuosities values seem reasonable since the observed range for porous sintered ceramics is usually

Table 6
Tuned model parameters.

Parameter	Value
Anode tortuosity for H_2 (τ_{H_2})	7.9
Anode tortuosity for other gases (τ_{an})	5.5
β in Eq. (22) (Ω^{-1} m^{-2})	1.26E9
Transfer coefficient (α)	0.33

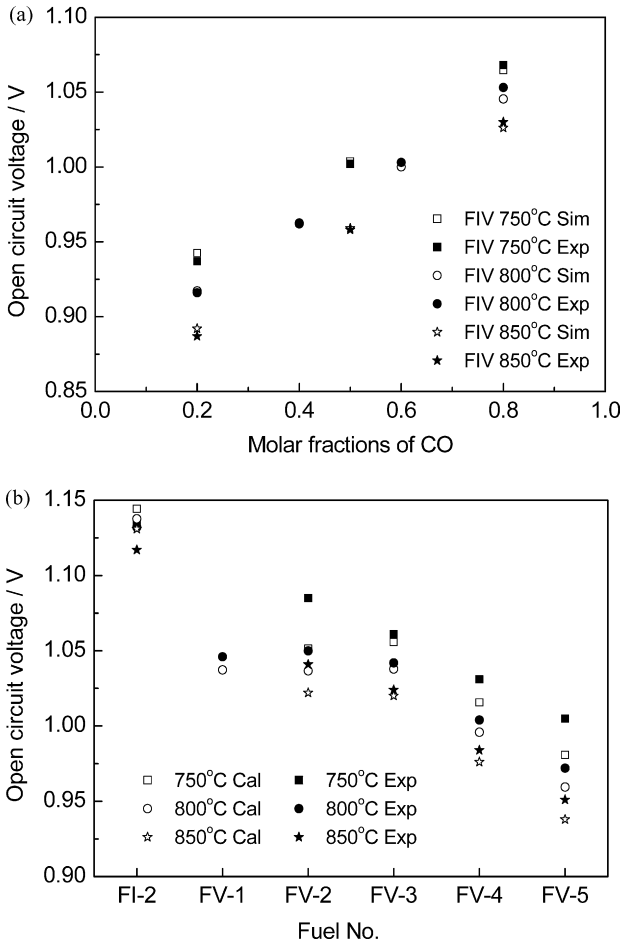

Fig. 4. A comparison of experimental observed OCVs and those calculated by model for various fuel mixtures (a) CO/CO_2, (b) H_2/H_2O and $H_2/H_2O/CO/CO_2$.

2–10, and most often in the range of 2–6 [50]. The transfer coefficient α depends on the symmetry of the activation barrier. For most electrochemical reactions, α ranges from 0.2 to 0.5 [42]. Once all the model parameters are determined, they were not changed in other cases simulations.

4.3. Model validation and discussion

4.3.1. Validations of open circuit voltages

To validate the capability of the model in prediction of OCVs, the calculated results based on equilibrium oxygen partial pressure mechanism were compared with the experimentally observed OCVs for various fuel compositions, which are shown in Fig. 4. Fig. 4(a) indicates that the calculated OCVs agree well with the experimental observations for CO/CO_2 fuel mixtures at all temperatures. Both the predicted and the experimental results show that the OCVs increase with the increasing of CO content and the decreasing of temperature. Fig. 4(b) shows a fairly good agreement between the calculated results and experimental data. For H_2/H_2O fuel mixtures, the experimental observed OCVs are slightly lower than calculated results presumably due to the slight gas leaks in cell testing. For $H_2/H_2O/CO/CO_2$ fuel mixtures, the experimental observed OCVs are slightly higher than those calculated by model, which are different from most results calculated by Nernst equation [8,24]. Nevertheless, it should be noted that the results are in good agreement with experiments for $H_2/H_2O/CO/CO_2$ fuel mixtures and the simplification that H_2 being assumed the only electrochemically active species for OCVs calculations is avoided. In addition, the

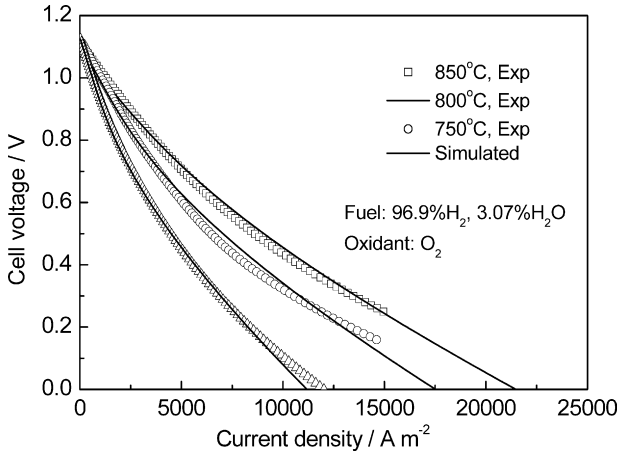

Fig. 5. Modeling and experimental polarization curves for H_2/H_2O fuel mixtures at 750, 800 and 850 °C. H_2 was humidified at 25 °C, corresponding to water content 3.07%.

fuel composition in actual test is not exactly the same as supposed, which maybe result in deviation.

For pure H_2, H_2/CO and H_2/CO_2 fuel mixtures, the contents of resident product gas (e.g. H_2O, CO_2) in actual testing are not exactly zero and hard to determine, which affect the OCVs significantly. Therefore, the calculations and comparisons of OCVs in these cases are not performed here.

In the validations of the model for various fuel mixtures, which are discussed in details as follows, the experimental observations are used as the OCVs in calculations. However, in the simulations and analyses of other fuels absent in experiments, the OCVs calculated by model are adopted.

4.3.2. Validations for H_2/H_2O fuel mixtures

Fig. 5 shows the experimental and simulated cell performances using H_2 humidified at 25 °C as fuel at 750, 800 and 850 °C. It is noted that the current densities of experiments are limited to about 15,000 A m^{-2} because the maximum allowed current of the electrochemical workstation (IM6ex, Zahner-Elektrik GmbH, Germany) is 2 A and the corresponding cathode area is 1.33 cm^2. Both the experimental and simulated data suggest that, as the operation temperature decreases, the cell performance deteriorates but the OCV increases. Fig. 5 indicates that the simulated polarization curves agree well with the experimental data at various temperatures. But the model slightly underestimates the cell performances at high current density.

4.3.3. Validations for H_2/CO and H_2/CO_2 fuel mixtures at 800 °C

The simulated results agree well with experimental data for all H_2/CO cases and the H_2/CO ratio has little influence to the OCVs. Besides, as the H_2/CO ratio increases, the cell operation voltage increases at a given current density, which is more significant at high current density. However, the influence of H_2/CO ratio to the cell performance is comparatively small from the overall.

Fig. 6 depicts the simulated and experimental polarization curves for various H_2/CO_2 fuel mixtures and shows a good agreement when the CO_2 content was up to 60% at 800 °C. However, the model results deviates from the experimental data and underestimate the diffusion transport at higher current density in 80% CO_2 case. As discussed in literature [50], for high current density and low H_2 concentration, the competitive adsorption and surface diffusion mechanism may be significant, which result in the increasing of diffusion resistance. Here the elementary reactions are used for gas adsorption and desorption processes. However, the model does not take into account the effect of surface diffusion, which may result

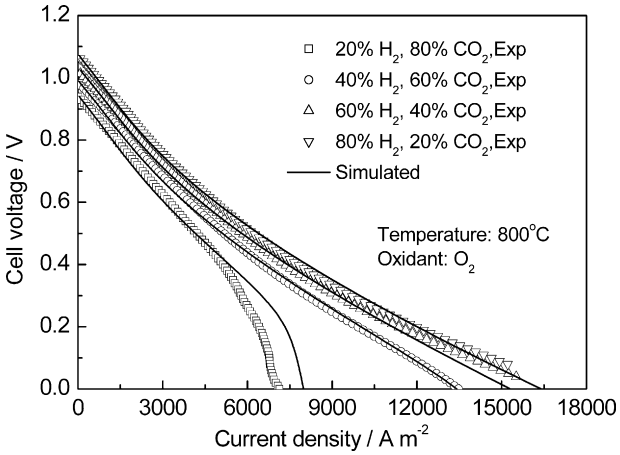

Fig. 6. Modeling and experimental polarization curves for various H_2/CO_2 fuel mixtures at 800 °C.

in the difference between experimental and simulated results at high current densities.

4.3.4. Validations for CO/CO_2 fuel mixtures

Fig. 7 shows the modeling and experimental polarization curves for various CO/CO_2 fuel mixtures at 750/800/850 °C. It can be observed from Fig. 7(b) that the modeling polarization curves agree well with the experimental data at 800 °C, the cases of which are the base cases for the model calibration. As the CO concentration decreases, the OCVs and cell performance decrease significantly. It is clear that there is a limiting current density at zero voltage caused by anodic concentration polarization. The simulated limiting current density is 11,193 A m^{-2} for 80% CO fuel mixture while 3940 A m^{-2} for 20% CO, which match well the values measured experimentally. The anodic concentration polarization is more significant and the cell operation voltage at turning point in polarization curve increases with the decreasing of CO content.

The polarization curves at 750 and 850 °C have the similar fuel compositions effects features compared with that at 800 °C. At 750 and 850 °C, the modeling results agree well with the experimental data at low current density but deviate from experimental data for some cases at high current density, which is shown in Fig. 7(a) and (c). The modeling results at 750 °C underestimate the diffusion resistance of concentration polarization slightly at high current density. For higher CO content (e.g. >50%) at 750 °C, the concentration polarization is not significant. The calculated limiting current densities are lower than experimental data at 850 °C, which is more pronounced in high CO content cases. The model overestimates the diffusion resistance of concentration polarizations, especially at higher current density. The simplification of model geometry might be an unneglectable derivation source. The anode of button cell is larger than the cathode, which results in the significant non-uniform distributions of gas concentrations in anode in radial direction. In fact, the model is not exactly accorded with 1D geometry assumption and this assumption will cause the deviation in calculations. The larger anode is helpful to the gas diffusions and enhances the performance of cell, especially for the high current density and significant concentration polarization situations. It should be noted that this effect is more remarkable for the gas with lower diffusion coefficients, such as CO and CO_2 compared to H_2 and H_2O. Comparison between the modeling results and experimental data in Fig. 7(a)–(c) indicates that the cell performance increases and concentration polarization becomes more significant with the increasing of temperature for the same CO/CO_2 composition. Therefore, the influence of geometry simplification is more obvious at 850 °C, which is shown in Fig. 7(c). In addition, the

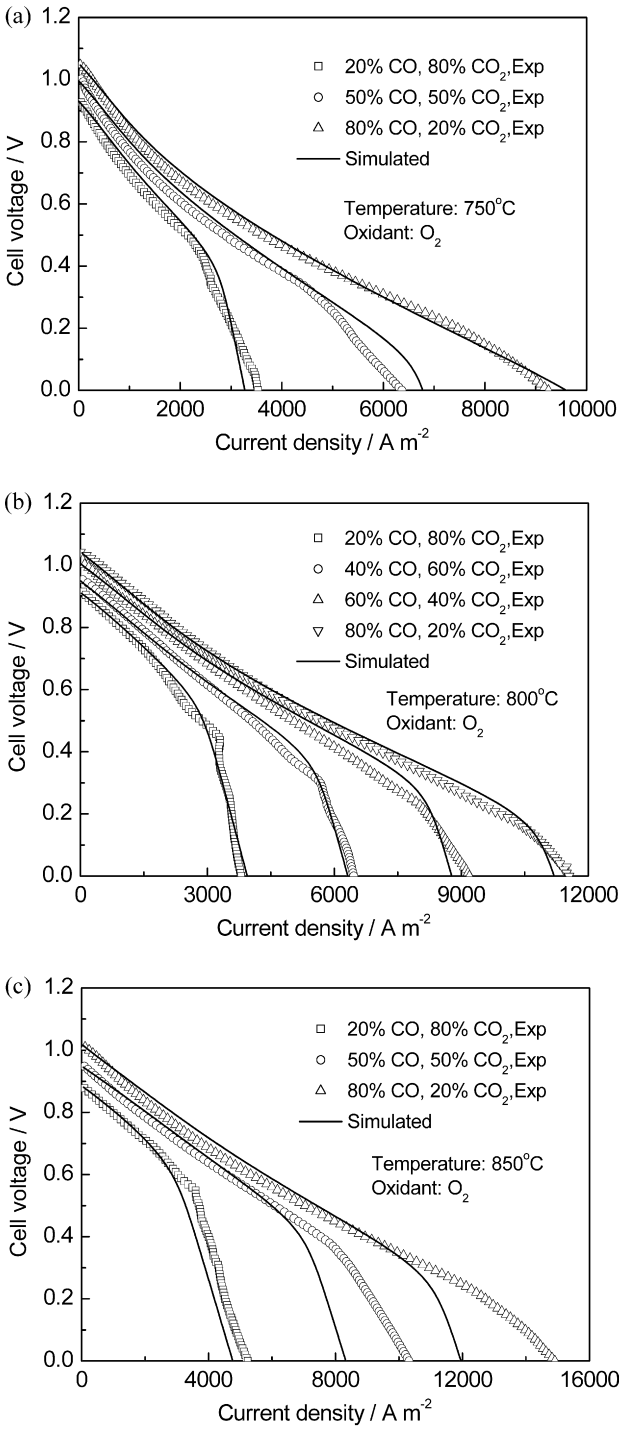

Fig. 7. Modeling and experimental polarization curves for various CO/CO_2 fuel mixtures (a) 750 °C, (b) 800 °C and (c) 850 °C.

neglect of bulk diffusion in anode chamber also enlarges the deviation of the calculated results from the experimental data at high current density.

4.3.5. Validations for $H_2/H_2O/CO/CO_2$ fuel mixtures

The comparison of experimental and simulated polarization curves is shown in Fig. 8 for various $H_2/H_2O/CO/CO_2$ fuel mixtures at 750/800/850 °C. In all cases, the fuel gas is saturated at 25 °C and the water content is kept at 3.07%. Both modeling and experimental results indicate that the cell performance increases with the decreasing of CO_2 content or the increasing of H_2/CO

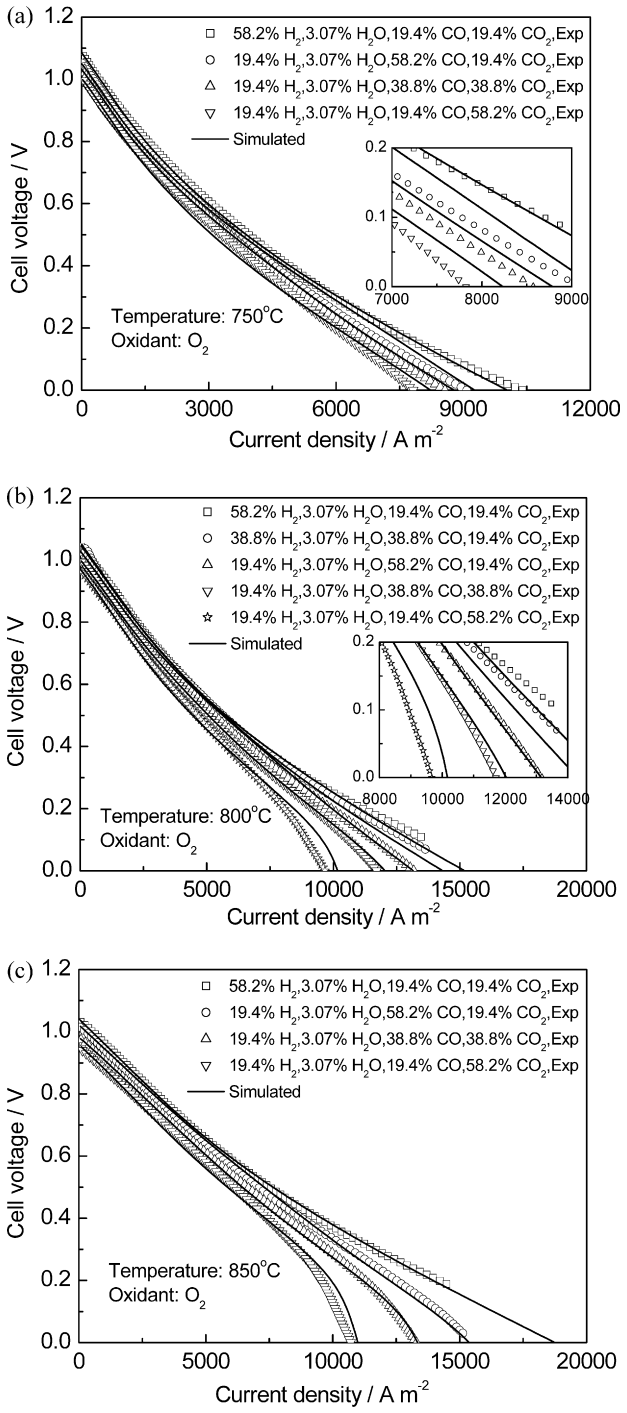

Fig. 8. Modeling and experimental polarization curves for various $H_2/H_2O/CO/CO_2$ fuel mixtures (a) 750 °C, (b) 800 °C and (c) 850 °C.

ratio at the same temperature. The increasing of temperature results in a higher OCV and a better cell performance for the same fuel gas composition. In addition, the concentration polarization becomes significant with raising temperature for high CO_2 content (e.g. >38.8%) cases at high current density. Fig. 8 shows a reasonable agreement between experimental and simulated polarization curves. It is proved that the model is comparably capable to calculate the performance of syngas fueled SOFC in a certain temperature range. However, there is still slight deviation of the simulated results from the experimental data. The simplification of gas diffusion in the model might be the major cause of the deviation.

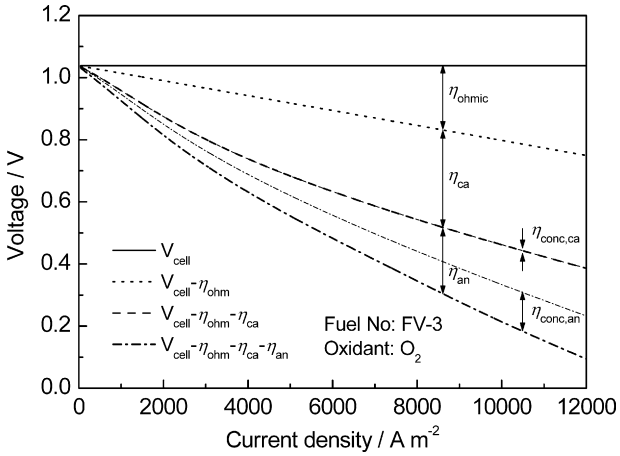

Fig. 9. Contributions of each PEN component to cell overpotential.

Suwanwarangkul et al. claimed that the DGM is more appropriate than EFM to simulated gas transport phenomena inside a SOFC anode by comparison [45], especially for multi-component gas diffusions. The calculation of effective diffusion coefficients in EFM is restricted to the situation wherein the species k diffuses in a mixture of stagnant and non-transferring species [44], which might cause the discrepancy for $H_2/H_2O/CO/CO_2$ fuel mixtures. In addition, the slight differences of cell ohmic resistance during testing also affect the agreements of simulated results and experimental data.

5. Simulation results and discussion

5.1. Cell overpotential

Numerous calculations have been carried out to predict the various cell overpotentials. Here the anodic and cathodic local overpotentials are defined as [8]

$$\eta_{an} = |(V_{elec|an\_sp/ac} - V_{ion|electrolyte/an\_act}) - V_{ref,an}| \quad (36)$$

$$\eta_{ca} = |(V_{elec|ca/cc} - V_{ion|electrolyte/ca}) - V_{ref,ca}| \quad (37)$$

The electrolyte overpotential, which includes the ohmic polarization and the loss due to contact resistance between the electrodes and electrolyte, is calculated as

$$\eta_{electrolyte} = (V_{ion|electrolyte/ca} - V_{ion|electrolyte/an\_act}) \quad (38)$$

Here the leak overpotential is neglected and then the total cell overpotential is calculated as

$$\eta_{total} = \eta_{an} + \eta_{ca} + \eta_{electrolyte} \quad (39)$$

In order to separate the effects of concentration overpotential, the source terms caused by electrochemical reactions of the anode and cathode mass balance equations (Eqs. (27)) are set to zero [8]. As a mathematical trick, then the oxidant concentrations are uniform in cathode and the fuel concentrations in anode only reflect the consumptions and productions of heterogeneous reactions without electrochemical reactions. In this way, the anodic and cathodic concentration overpotentials are obtained in simulations. Fig. 9 shows the simulated detailed contributions of each PEN component to the cell overpotential for FV-3 fuel mixture and pure oxygen at 800 °C.

The modeling results in Fig. 9 indicate that the cathodic activation overpotential and ohmic overpotential dominate for syngas fueled SOFC operating at 800 °C at low current density. Whereas the

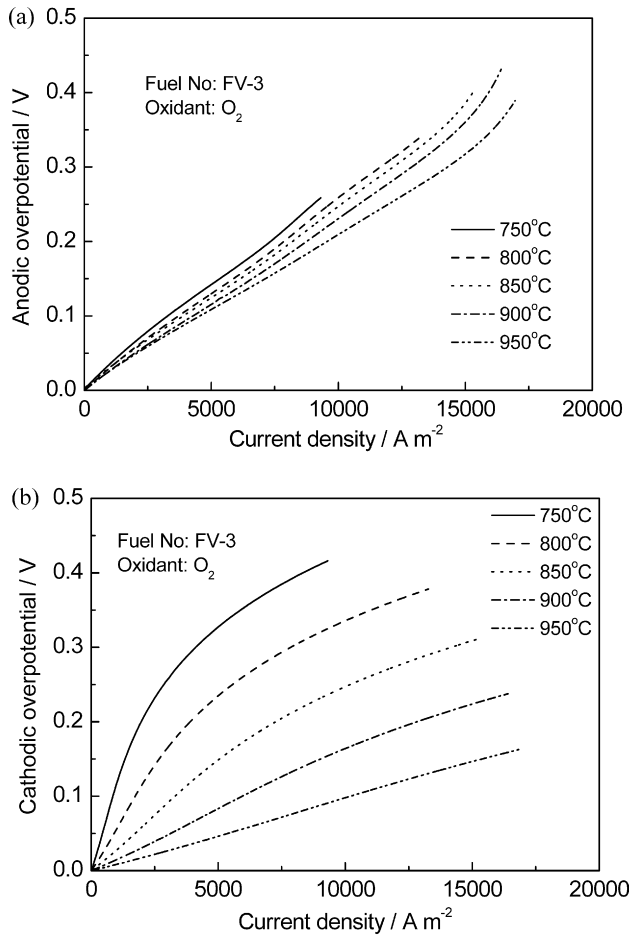

Fig. 10. Cell overpotentials as a function of current density for various operation temperatures in (a) anode and (b) cathode.

ratio of the anodic activation overpotential to the cell overpotential increases with the current density. The cathodic concentration polarization in this case is neglectable because the cathode film is thin enough and pure oxygen is used as oxidant. In contrast, the anodic concentration polarization is more significant than that in cathode due to the thick anode. The anodic concentration overpotential increases with the current density and is more than 15% of total overpotential for current density above 12,000 A m^{-2}.

The effects of temperature on the anodic and cathodic overpotentials for FV-3 fuel mixture and pure oxygen at various temperatures are shown in Fig. 10. It is clear that the operation temperature affects both the anodic and cathodic overpotential and the overpotentials in both electrodes increase as the temperature decreases, as expected. The anodic overpotentials increase with current density linearly at low current density and increase rapidly when current density is more than 15,000 A m^{-2}, which is caused by the significant concentration polarization. The effects of temperature on overpotentials are more pronounced in cathode than in anode. Therefore, the anodic activation overpotentials dominate for SOFC operation at high temperature. Besides, it should be noted that the cathodic overpotentials increase rapidly at low current density but relatively slow at high current density for low temperature cases (such as 750 and 800 °C). So the fraction of anodic overpotential to cathodic overpotential increases at first then decrease with current density, which also can be observed in Fig. 9.

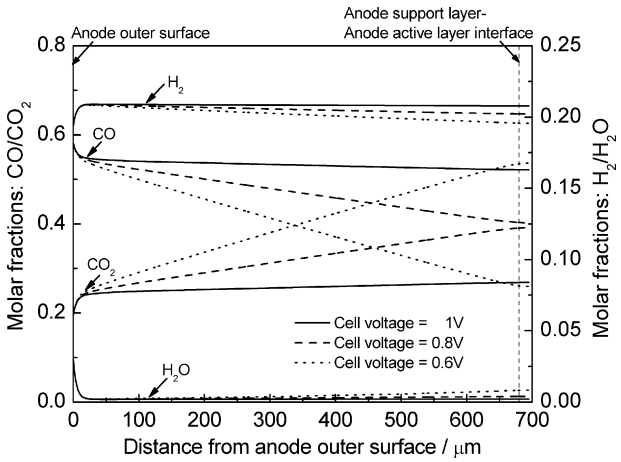

Fig. 11. Molar fractions distributions of $H_2/H_2O/CO/CO_2$ in anode.

5.2. Species concentration distributions in anode

5.2.1. Effects of operation voltage

Fig. 11 shows the H_2, H_2O, CO and CO_2 molar fractions distributions in the anode for FV-3 fuel mixture and pure oxygen at 800 °C with cell voltage 1, 0.8 and 0.6 V. It can be seen that the concentrations of H_2 and CO_2 increase while those of H_2O and CO decrease rapidly to the equilibrium near the anode outer surface for all the cell voltages. The heterogeneous reactions of syngas in anode are quick enough. Once the gaseous species diffuse into the anode, the gases concentrations reach equilibrium rapidly (less than 50 μm from anode outer surface). In addition, the concentrations of H_2 and CO decrease in the anode from the heterogeneous reactions equilibrium point to the anode-active layer/electrolyte interface, while the opposite is true for H_2O and CO_2. This is due to the electrochemical reactions at the TPB which results in the consumption of H_2 and CO and production of H_2O and CO_2. The calculated results show that the operation voltage significantly affects the gas concentrations. As the operation voltage decreases, the cell current density increases and electrochemical reactions rates increase, which accelerates the H_2/CO consumptions and H_2O/CO_2 productions, especially near the electrolyte. It should be noted that the variations of CO/CO_2 concentrations are more obvious than those of H_2/H_2O because the water–gas-shift reaction turns H_2O and CO to H_2 and CO_2.

Fig. 12 shows the coverage distributions of various surface species in the anode for FV-3 fuel mixture, pure oxygen at 800 °C with cell voltage 1, 0.8 and 0.6 V. It can be seen that CO(s), H(s) and Ni(s) (Ni vacancies) are the major species in anode; C(s), O(s), CO_2(s), H_2O(s) and OH(s) are the minor species in anode, the coverage of which is about 10^{-5} to 10^{-6}. Due to the rapid heterogeneous reactions, the surface species reach equilibrium quickly near the anode outer surface as gaseous species, which is more significant for minor surface species. The coverage of O(s), CO_2(s), H_2O(s) and OH(s) decreases but that of C(s) increases sharply and reaches equilibrium in less than 50 μm from anode outer surface. Then the surface species in anode will be uniform from the equilibrium point to the electrolyte at OCV. As the cell voltage decreases and current density increases, the electrochemical reactions in anode are accelerated, especially in the regime near electrolyte. Then the acceleration of electrochemical reactions results in the increasing of H(s), Ni(s), O(s), CO_2(s), H_2O(s), OH(s) and the decreasing of CO(s), C(s) at low cell voltage. The closer to the electrolyte in anode, the more significant the effects of cell voltage on surface species coverage are. Besides, it should be noted that the carbon deposition mitigates along the anode thickness

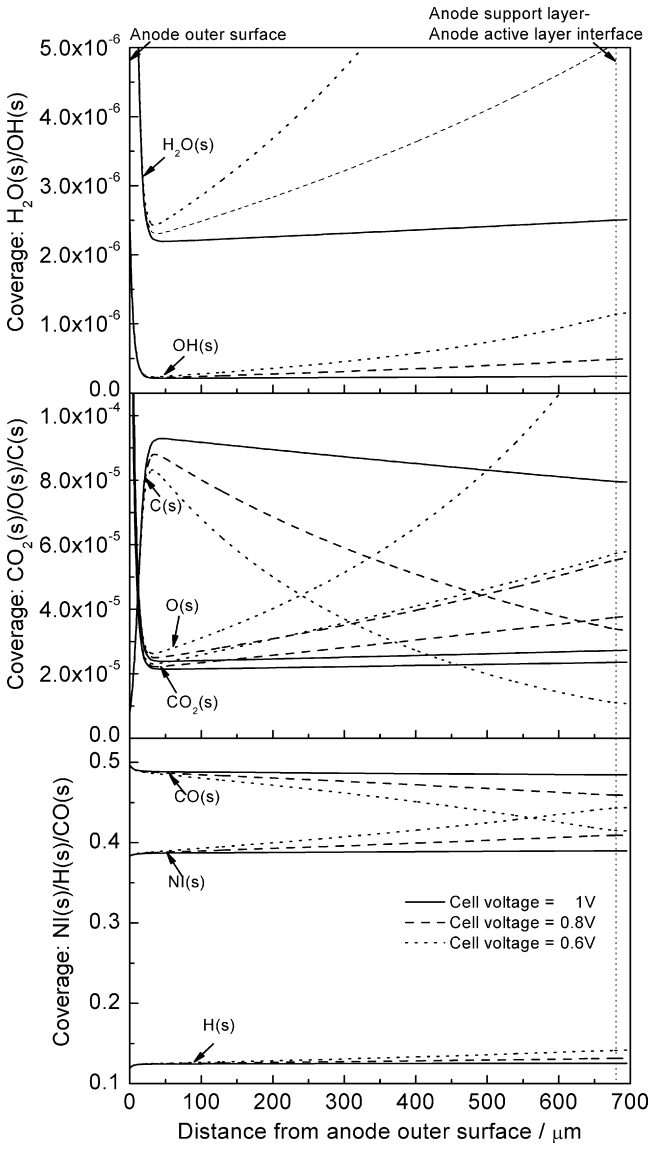

Fig. 12. Coverage distributions of various surface species in anode.

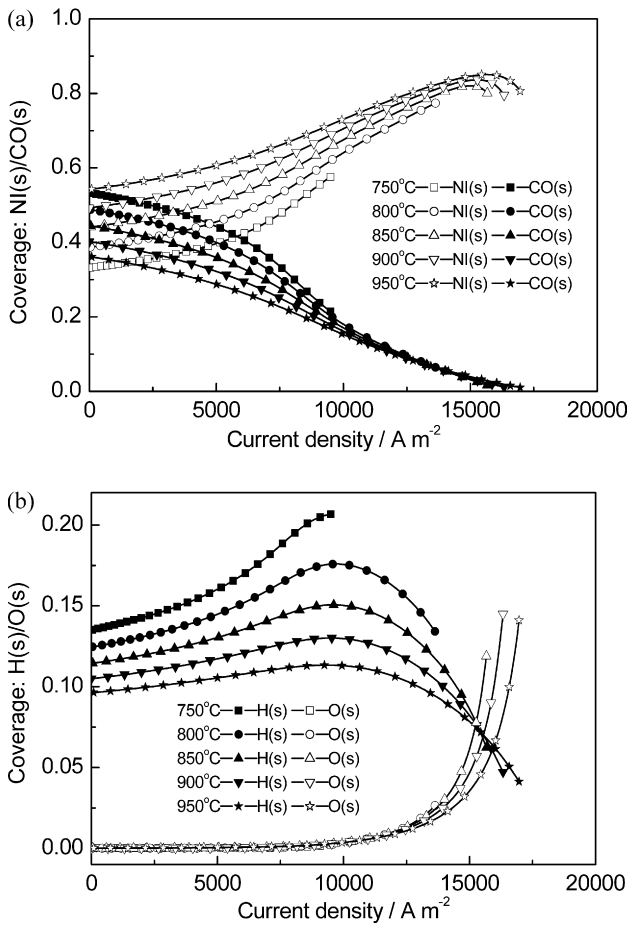

Fig. 13. The surface coverage of (a) Ni(s) and CO(s), and (b) H(s) and O(s) as a function of current density for various operation temperatures. All data for FV-3 fuel mixture, pure oxygen and the point of anode-support layer/anode-active layer interface.

direction from anode outer surface to electrolyte at a given cell voltage.

5.2.2. Effects of operation temperature

Fig. 13 shows the effects of current density on the surface coverage of Ni(s), CO(s), H(s) and O(s) for various temperatures. With the increasing of the current density, the coverage of O(s) and Ni(s) increases; the coverage of CO(s) decreases; the coverage of H(s) increases at first then decreases, which reaches maximum at about 10,000 A m^{-2}. That is because more and more O(s) is formed from oxygen ionic by electrochemical reactions at high current density. As a minor intermediate species, the increasing of O(s) accelerates the heterogeneous reactions, which turn more CO(s) to CO_2(s) and produce free Ni surface. The effects of the increscent O(s) to the variation of H(s) are more complicated. The surface coverage of H(s) is determined by heterogeneous reactions (11)–(16). Due to the concentration polarizations, the coverage of Ni(s) decreases slightly and that of O(s) increases sharply when current density is more than 16,000 A m^{-2}, which is more significant for high temperatures (e.g. above 850 °C). Besides, it should be noted that the coverage of H(s), CO(s) and O(s) decreases with increasing temperature at a given current density. That is because the desorption rates are higher at high temperature and thereby leaving more free Ni surface.

5.3. Current density distributions

The simulation results indicate that the cell voltage significantly affects the electronic current density, which increases with the decreasing of cell voltage. The electronic current density distribution reflects the degree of electrochemical reactions, which are mainly concentrated in the zone where the slope of electronic current density distribution is large. The simulated cathodic current density distributions indicate that the electrochemical reactions occurred within the whole cathode uniformly. Therefore, an appropriate thicker cathode is helpful to improve the cell performance due to the increasing of TPB active sites for cathodic electrochemical reactions.

Fig. 14 gives the electronic current density distributions within the anode along the cell thickness direction for FV-3 fuel mixture, pure oxygen at 800 °C with cell voltage 1, 0.8 and 0.6 V. It can be seen that the anodic electrochemical reactions are mainly distributed within a 50 μm distance from the anode-active layer/electrolyte interface. It is easily concluded from the curve slopes that the electrochemical reactions rates in anode-active layer are larger than those in anode-support layer. That is because there are a better ionic conductivity and more TPB active sites per unit volume in the anode-active layer. In addition, the electrochemical reactions are also not limited within the anode-active layer and extent to the anode-support layer. However, there are no obvious electro-

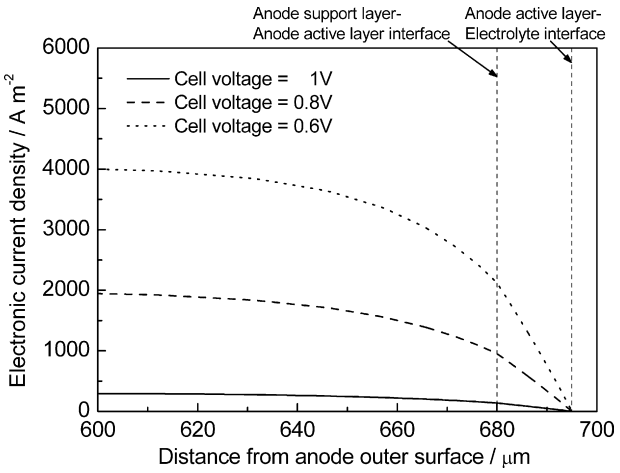

Fig. 14. Electronic current density distribution in anode near the electrolyte.

chemical reactions for a large range in the middle of anode-support layer.

5.4. Effects of carbon deposition in anode

The surface coverage distribution of deposited carbon in anode has been given in Fig. 12 and discussed in detail in Section 5.2. Here a point of anode-support layer/anode-active layer interface in anode is taken for example to study the effects of temperature, current density and fuel composition on carbon depositions.

Fig. 15 shows the carbon deposition as a function of current density for various operation temperatures for FV-3 fuel mixture and pure oxygen. It is evident from the figure that the carbon deposition is mitigated at high current density for all temperatures. It is mainly because that, as the current density increases, more surface specie O(s) is produced by electrochemical reactions and hence reducing the possibility of carbon deposition on Ni surfaces by Bouduard reactions. Besides, as the temperature decreases, the surface coverage of C(s) increases significantly at a given current density. The effect of temperature on carbon deposition is more pronounced at low current density, but the degree of carbon deposition trends to be identical for various temperatures with the increasing of current density. Therefore, the carbon deposition of syngas fueled SOFC could be reduced by raising the operation temperature and reducing cell voltage.

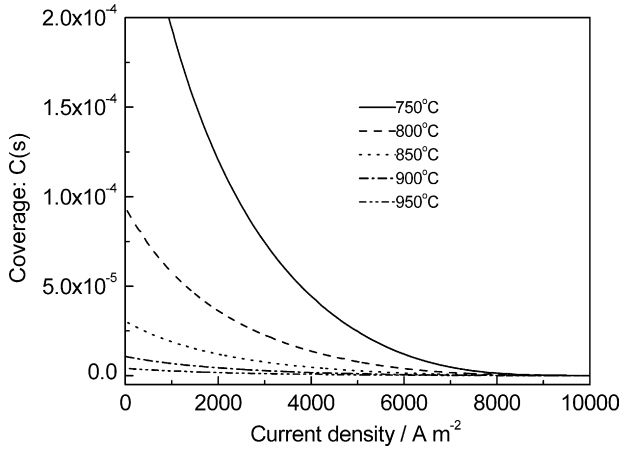

Fig. 15. Carbon deposition as a function of current density for various operation temperatures. All data for FV-3 fuel mixture, pure oxygen and the point of anode-support layer/anode-active layer interface.

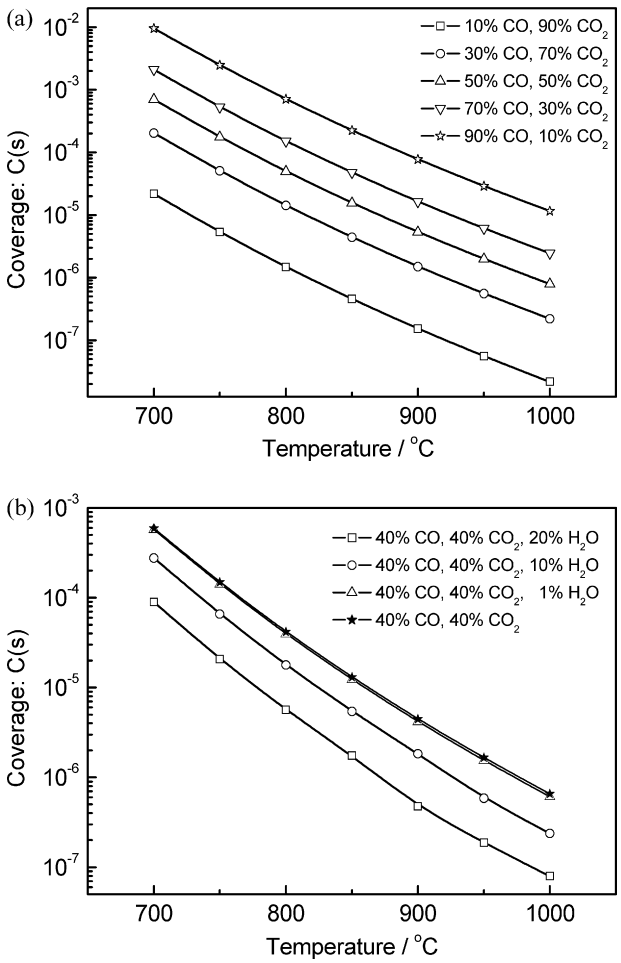

Fig. 16. Effects of fuel compositions on carbon deposition for various (a) CO/CO_2 ratios and (b) H_2O contents. All data for a cell voltage of OCV and the point of anode-support layer/anode-active layer interface.

Fig. 16 highlights the effects of fuel compositions on carbon deposition at OCV. Therefore, the effects of current density are excluded. The results of Fig. 16(a) indicate that, as the CO content increases, the degree of carbon deposition aggravates for CO/CO_2 fuel mixture. Fig. 16(b) shows the effects of H_2O content in fuel mixtures on carbon depositions for 40% CO and 40% CO_2, respectively. N_2 is used as dilution in the fuel mixtures. The addition of H_2O in the fuel mixture improves the resistance of carbon deposition greatly, especially for higher H_2O content (e.g. more than 10%). However, the existence of H_2 in fuel mixture has insignificant effect on carbon deposition, which mainly caused by the H_2O produced through electrochemical reactions. Furthermore, the carbon deposition in all cases in Fig. 16 shows the expected behavior with the temperature, which has been discussed earlier.

5.5. Effects of typical syngas on cell performances

For actual SOFC operation, the fuel syngas is a mixture of H_2 and CO produced mainly from coal or natural gas via various chemical processes. However, different fossil fuels and chemical processes lead to different syngas compositions, which affect the cell performances significantly. Therefore, the effects of typical syngas on cell performance from two most commonly used syngas production processes are discussed here. The first aspect involves the coal-derived syngas produced from coal gasifier. The second analysis relates to the syngas from thermochemical reforming techniques.

Table 7
Syngas compositions of typical entrained-flow coal gasifier [51].

Gasifier	Coal	Syngas compositions (vol%)								
		H_2	H_2O	CO	CO_2	CH_4	Ar	N_2	H_2S	COS
Texaco	Illinois 6	30.28	16.45	39.58	10.78	0.08	0.91	0.73	1.00	0.03
Shell	Illinois 6	26.74	2.01	63.05	1.49	0.03	1.1	4.08	1.3	0.14
	Texas lignite	27.57	3.2	60.63	2.77	0.03	1.03	4.34	0.32	0.04
Destec	Texas lignite	24.6	34.64	21.81	17.15	0.03	0.78	0.54	0.25	0.01

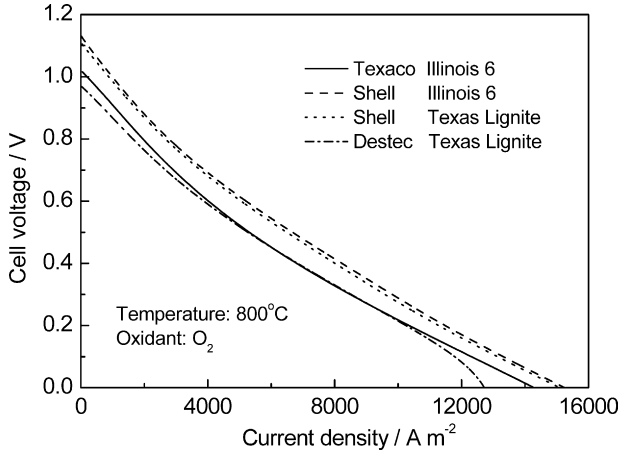

Fig. 17. Cell performances fueled by the syngas of typical entrained-flow coal gasifier at 800 °C.

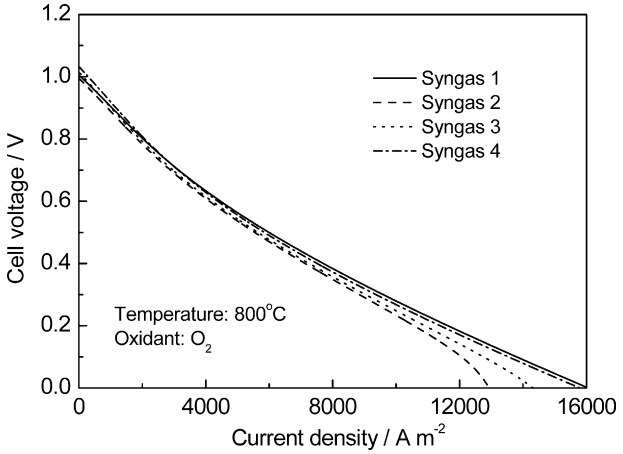

Fig. 18. Cell performances fueled by the syngas of typical methane thermochemical reforming at 800 °C.

Compared with combustion, coal gasification is only partial oxidation producing combustible fuel gas. The classic gasifier could be divided into three types: moving-bed gasifier, fluidized-bed gasifier and entrained-flow gasifier [51]. Due to the large production capacity, wide fuel adaptability and stable operation property, the entrained-flow gasifier is selected here. Table 7 lists the syngas compositions of typical entrained-flow coal gasifier.

The CH_4, Ar, H_2S and COS in syngas are neglected and treated as N_2 in calculations due to the minor content compared to other gas. Fig. 17 shows the cell performances fueled by the syngas of typical entrained-flow coal gasifier at 800 °C. The results indicate that the cell performance and OCV increase with the increasing of effective compositions (e.g. H_2 and CO) in fuel. The effective compositions in syngas of Texaco and Destec gasifier are 69.9% and 46.4%, respectively, whereas those of Shell gasifier are more than 82.2% for two kinds of coal. Therefore, the performances of the cells fueled with the syngas of Shell gasifier are better than that of Texaco or Destec gasifier. However, it should be noted that the CO content in the syngas of Shell gasifier is relatively high whereas the H_2O content is low, which may cause carbon deposition. Besides, it is clear that there is concentration polarization for the syngas of Destec gasifier at high current density due to the low effective compositions.

Another common syngas production process is the thermochemical reforming from hydrocarbon fuels. There are three major thermochemical reforming techniques used to produce syngas, i.e. steam reforming (SR), partial oxidation (POX), and autothermal reforming (ATR) [52]. Here the syngas compositions and operation conditions of typical methane thermochemical reforming are listed in Table 8. In calculations, the minor gas component CH_4 is neglected and treated as N_2.

Fig. 18 shows the cell performance fueled by the syngas of typical methane thermochemical reforming at 800 °C. There is no obvious

Table 8
Syngas compositions and operation conditions of typical methane thermochemical reforming.

Molar fraction (%)	Syngas 1 [53]		Syngas 2 [54]		Syngas 3 [55]		Syngas 4 [52]	
	(SR)		(POX)		(POX)		(ATR)	
	Inlet	Outlet	Inlet	Outlet	Inlet	Outlet	Inlet	Outlet
H_2	0	55.6	0	29.8	0	35.2	0	50.0
H_2O	74.8	26.6	26.7	20.2	22.7	14.0	26.0	19.5
CO	0	9.2	0	9.2	0	10.5	0	25.0
CO_2	0	7.2	0	5.1	0	5.4	5.2	5.2
CH_4	23.0	0.7	19.1	0.9	22.7	1.7	43.3	0.3
N_2	2.2	0.7	42.9	34.8	43.1	33.2	0	0
O_2	0	0	11.4	0	11.5	0	25.5	0
Temperature (°C)	565	700	535	867	720	640	427	1050
Pressure (MPa)	0.115		2.53	2.48	0.8		2.1	
Catalyst	Ni-based		$Ni/MgO/Al_2O_3$		Ni-based		Ni-based	
Steam carbon ratio	3.25		1.40		1		0.6	
Oxygen carbon ratio	0		0.597		0.504		0.59	
CH_4 conversion (%)	96.3		93.6		90.5		/	

difference in cell performance for all the syngas, especially at low current density. The effective compositions in syngas 1 to syngas 4 are 64.8%, 39.0%, 45.7% and 75%, respectively. For syngas 2 and 3, due to the large N_2 content introduced by using air as oxidant, the effective compositions are diluted. Therefore, the cell performance is relatively low and there is a concentration polarization at high current density. Besides, the H_2 content in methane-derived syngas is more than that in coal-derived syngas, which results in higher performance for same effective compositions and mitigation of carbon deposition.

6. Conclusion

A detailed one-dimension transient elementary reaction kinetic model of an SOFC operating with syngas based on button cell geometry was developed. The model, which incorporated anodic elementary heterogeneous reactions, electrochemical kinetics, electrodes microstructure and complex transport phenomena (momentum, mass and charge transport) in cell, was validated with experimental performance for various syngas compositions at 750, 800 and 850 °C. The comparisons show that the model agrees reasonably well with the experimental data.

The simulation results indicate that the cathodic activation overpotential and ohmic overpotential dominate at low temperature while the anodic activation overpotential is more significant at high temperature. The anodic concentration polarization increases with current density and is more than 15% of total overpotential when current density is above 12,000 A m^{-2} for FV-3 fuel mixture. Besides, the electrochemical reactions are condensed in the anode-active layer and neighbouring support layer for anode. For the heterogeneous reactions, CO(s), H(s) and Ni(s) (Ni vacancies) are the major species in anode; C(s), O(s), CO_2(s), H_2O(s) and OH(s) are the minor species, of which the coverage is about 10^{-5} to 10^{-6}. As the cell voltage decreases and current density increases, H(s), Ni(s), O(s), CO_2(s), H_2O(s), OH(s) increases but CO(s) and C(s) decrease. The coverage of H(s), CO(s) and O(s) decreases with increasing temperature and leaving more free Ni surface. Afterwards, the modeling results indicate that higher temperature and lower operation voltage are helpful to reduce the possibility of carbon deposition on Ni surfaces by Bouduard reactions. In addition, as the CO_2 and H_2O contents in syngas increase, the degree of carbon deposition aggravates. Finally, the cell performance analysis of typical syngas from entrained-flow coal gasifier and methane thermochemical reforming processes indicates that the cell performance and OCV increase with the increasing of effective compositions (e.g. H_2 and CO) in fuel. The large N_2 content in syngas introduced by using air as oxidant leads to significant deterioration of performance.

Acknowledgements

The authors acknowledge the Project 20776078 supported by National Natural Science Foundation of China and the Project 20080440033 supported by China Postdoctoral Science Foundation. We gratefully acknowledge the insightful discussions and offers of button cells used in experiments from Prof. Shaorong Wang in Shanghai Institute of Ceramics Chinese Academy of Sciences (SICCAS), China.

References

[1] S.C. Singhal, K. Kendall, High Temperature Solid Oxide Fuel Cells: Fundamentals, Design and Applications, Elsevier Advance Technology, Oxford, UK, 2003.
[2] J.H. Hirschenhofer, D.B. Stauffer, R.R. Engleman, et al., Fuel Cell Handbook, seventh ed., EG&G Technical Services, Inc., West Virginia, 2004.
[3] K. Sasaki, Y. Hori, R. Kikuchi, K. Eguchi, A. Ueno, H. Takeuchi, M. Aizawa, K. Tsujimoto, H. Tajiri, H. Nishikawa, Y. Uchida, J. Electrochem. Soc. 149 (2002) A227–A233.
[4] S. Baron, N. Brandon, A. Atkinson, B. Steele, R. Rudkin, J. Power Sources 126 (2004) 58–66.
[5] S. Onuma, A. Kaimai, K. Kawamura, Y. Nigara, T. Kawada, J. Mizusaki, H. Tagawa, Solid State Ionics 132 (2000) 309–331.
[6] K. Eguchi, H. Kojo, T. Takeguchi, R. Kikuchi, K. Sasaki, Solid State Ionics 152–153 (2002) 411–416.
[7] A. Weber, B. Sauer, A. Muller, D. Herbstritt, E. Ivers-Tiffee, Solid State Ionics 152–153 (2002) 543–550.
[8] Y.X. Shi, N.S. Cai, C. Li, C. Bao, E. Croiset, J.Q. Qian, Q. Hu, S.R. Wang, J. Power Sources 172 (2007) 235–245.
[9] Y.X. Shi, N.S. Cai, C. Li, C. Bao, E. Croiset, J.Q. Qian, Q. Hu, S.R. Wang, J. Power Sources 172 (2007) 246–252.
[10] Y.X. Shi, N.S. Cai, C. Li, J. Power Sources 164 (2007) 639–648.
[11] K.P. Recknagle, R.E. Williford, L.A. Chick, D.R. Rector, M.A. Khaleel, J. Power Sources 113 (2003) 109–114.
[12] H. Yakabe, T. Sakurai, Solid State Ionics 174 (2004) 295–302.
[13] N. Autissier, D. Larrain, J. Van herle, D. Favrat, J. Power Sources 131 (2004) 313–319.
[14] T. Nishino, H. Iwai, K. Suzuki, J. Fuel Cell Sci. Technol. 3 (2006) 33–44.
[15] J. Yuan, B. Sunden, J. Fuel Cell Sci. Technol. 3 (2006) 89–98.
[16] R. Suwanwarangkul, E. Croiset, E. Entchev, S. Charojrochkul, M.D. Pritzker, M.W. Fowler, P.L. Douglas, S. Chewathanakup, H. Mahaudom, J. Power Sources 161 (2006) 308–322.
[17] T. Aloui, K. Halouani, Appl. Therm. Eng. 27 (2007) 731–737.
[18] R.S. Gemmen, J. Trembly, J. Power Sources 161 (2006) 1084–1095.
[19] Y. Xie, X. Xue, Int. J. Hydrogen Energy (2009), doi:10.1016/j.ijhydene.2009.06.034.
[20] E.S. Hecht, G.K. Gupta, H. Zhu, A.M. Dean, R.J. Kee, L. Maier, O. Deutschmann, Appl. Catal. A 295 (2005) 40–51.
[21] H. Zhu, R.J. Kee, J. Electrochem. Soc. 153 (2006) A1765–A1772.
[22] W.G. Bessler, S. Gewies, M. Vogler, Electrochim. Acta 53 (2007) 1782–1800.
[23] H. Zhu, A.M. Golclasure, R.J. Kee, Y. Lin, S.A. Barnett, J. Power Sources 161 (2006) 413–419.
[24] V.M. Janardhanan, O. Deutschmann, J. Power Sources 162 (2006) 1192–1202.
[25] H. Zhu, R.J. Kee, M.R. Pillai, S.A. Barnett, J. Power Sources 183 (2008) 143–150.
[26] V.M. Janardhanan, V. Heuveline, O. Deutschmann, J. Power Sources 172 (2007) 296–307.
[27] V.M. Janardhanan, O. Deutschmann, Chem. Eng. Sci. 62 (2007) 5473–5486.
[28] G.M. Goldin, H. Zhu, R.J. Kee, D. Bierschenk, S.A. Barnett, J. Power Sources 187 (2009) 123–135.
[29] A. Bieberle, L.J. Cauckler, Solid State Ionics 146 (2002) 23–41.
[30] S.P. Jiang, S.P.S. Badwal, J. Electrochem. Soc. 144 (1997) 3777–3784.
[31] B. de Boer, SOFC Anode: Hydrogen Oxidation at Porous Nickel and Nickel/Yttria Stabilized Zirconia Cermet Electrodes, Ph.D. thesis, University of Twente, The Netherlands, 1998.
[32] P. Holtappels, I.C. Vinke, G.J. de Haart, U. Stimming, J. Electrochem. Soc. 146 (1999) 2976–2982.
[33] W.G. Bessler, J. Warnatz, D.G. Goodwin, Solid State Ionics 177 (2007) 3371–3383.
[34] A.M. Sukeshini, B. Habibzadeh, B.P. Becker, C.A. Stoltz, B.W. Eichhorn, G.S. Jackson, J. Electrochem. Soc. 153 (2006) A705–A715.
[35] Y. Matsuzaki, I. Yasuda, J. Electrochem. Soc. 147 (2000) 1630–1635.
[36] Y.X. Shi, N.S. Cai, C. Li, C. Bao, E. Croiset, J.Q. Qian, Q. Hu, S.R. Wang, J. Electrochem. Soc. 155 (2008) B270–B280.
[37] W.G. Bessler, Solid State Ionics 176 (2005) 997–1011.
[38] R.J. Kee, M.E. Coltrin, P. Blarborg, Chemically Reacting Flow, John Wiley & Sons. Inc., Hoboken, NJ, 2003.
[39] V.M. Janardhanan, V. Heuveline, O. Deutschmann, J. Power Sources 178 (2008) 368–372.
[40] P. Costamagna, P. Costa, V. Antonucci, Electrochim. Acta 43 (1998) 375–394.
[41] S.H. Chan, Z.T. Xia, J. Electrochem. Soc. 148 (2001) A388–A394.
[42] R.P. O'Hayre, S.W. Cha, W. Colella, F.B. Prinz, Fuel Cell Fundamentals, John Wiley & Sons, Inc., Hoboken, NJ, 2006.
[43] R. Krishna, J.A. Wesselingh, Chem. Eng. Sci. 52 (1997) 861–911.
[44] E.A. Mason, A.P. Malinauskas, Gas Transport in Porous Media: The Dusty-Gas Model, Elsevier, New York, 1983.
[45] R. Suwanwarangkul, E. Croiset, M.W. Fowler, P.L. Douglas, E. Entchev, M.A. Douglas, J. Power Sources 122 (2003) 9–18.
[46] J. Divisek, R. Wilkenhoner, Y. Volfkovich, J. Appl. Electrochem. 29 (1999) 153–163.
[47] R.J. Braun, Optimal Design and Operation of Solid Oxide Fuel Cell Systems For Small-Scale Stationary Applications, Ph.D. thesis, University of Wisconsin, Madison, USA, 2002, pp. 109–111.
[48] J.H. Nam, D.H. Jeon, Electrochim. Acta 51 (2006) 3446–3460.
[49] A. Mitterdorfer, L.J. Gauckler, Solid State Ionics 117 (1999) 203–217.
[50] R.E. Williford, L.A. Chick, G.D. Maupin, S.P. Simner, J.W. Stevenson, J. Electrochem. Soc. 150 (2003) A1067–A1072.
[51] Electric Power Research Institute, Coal Gasification Guidebook: Status, Applications, and Technologies, Final report, 1993.
[52] M. Zahedi nezhad, S. Rowshanzamir, M.H. Eikani, Int. J. Hydrogen Energy 34 (2009) 1292–1300.
[53] G. Lozza, P. Chiesa, J. Eng. Gas Turbines Power 124 (2002) 89–95.
[54] A.M.D. Groote, G.F. Froment, Catal. Today 37 (1997) 309–329.
[55] S. Liu, W. Li, Y. Wang, H. Xu, Fuel Process. Technol. 89 (2008) 1345–1350.